# Supporting Information

# Depressing charge recombination in hybrid perovskites by introducing dynamic electron/energy relay couple towards enhanced photocatalytic hydrogen production

*Jiaqi Liu[a], Yuxin Xie[bc], Yongxin Jiao[a], Hefeng Zhang[a], Junhui Wang[d], Yuying Gao[c], and Xu Zong[a,]**

[a]Marine Engineering College, Dalian Maritime University, Linghai Road 1, Dalian 116026, China

[b]School of Chemistry and Materials Science, University of Science and Technology of China, Hefei 230026, China

[c]State Key Laboratory of Catalysis, Dalian National Laboratory for Clean Energy, Dalian Institute of Chemical Physics, Chinese Academy of Sciences, Dalian 116023, China

[d]State Key Laboratory of Molecular Reaction Dynamics, Dalian Institute of Chemical Physics, Chinese Academy of Sciences Dalian, Liaoning 116023, China

AUTHOR INFORMATION

**Corresponding Author**

*E-mail: xuzong@dlmu.edu.cn.

## Chemicals and materials

$PbI_2$ (99.999%), methylamine (MA, 40 wt% in absolute ethanol), cuprous iodide (CuI, 99.5%), $H_2PtCl_6 \cdot 6H_2O$, DMSO, and DMF were purchased from Sigma Aldrich. HI (57 wt%, unstabilized) and $H_3PO_2$ (50 wt %, in water) were purchased from Macklin. Diethyl ether was received from Sinopharm Chemical Reagent Co., Ltd. These chemicals and reagents were used as received without further purification.

## Synthesis of methylammonium iodide (MAI)

MAI was synthesized by the reaction of methylamine with HI solution. 15 mL MA was dropwise added into 15 mL of HI solution (57 wt % in water) and stirred in ice water bath for 1 h. The solvent was removed by rotary evaporation at 60 ℃ and the precipitate was washed repeatedly with diethyl ether. The precursors were dissolved in ethanol and recrystallized with diethyl ether. Finally, the produced MAI products were washed with diethyl ether and dried in a vacuum oven at 60 ℃ for 12 h.

## Synthesis of $MAPbI_3$ powder

The $MAPbI_3$ was prepared from by dissolving 0.645 mol $L^{-1}$ of $PbI_2$ and 0.645 mol $L^{-1}$ of MAI in 12 mL of HI solution and 4 mL $H_3PO_2$.The solution was heated at 100 °C for 1 h, then cooled to room temperature to obtain the $MAPbI_3$ perovskite precipitates. The $MAPbI_3$ perovskite precipitates were separated from the saturated solution by a centrifuge treatment and dried under vacuum at 60 °C for 48 h. The $MAPbI_3$ perovskite powders were used in photocatalytic $H_2$ evolution reactions.

## Preparation of perovskite and Pt/perovskites films

The perovskites films were used for surface photovoltage microscopy (SPVM) and transient absorption (TA) measurements. The perovskites films were prepared on quartz glass. The quartz glass was sequentially washed with 2 mol $L^{-1}$ KOH and deionized water for 10 min with sonication. The precursor solution was prepared by dissolving 0.3 mol $L^{-1}$ perovskites in 1 mL mixed solvent of DMF and DMSO (volume ratio of 4:1). 30 μL of precursor solution was spin-coated onto the quartz substrate, and then the sample was spun at 3000 r.m.p for 30 s, followed by annealing at 100 °C in air for 10 min.

**Photocatalytic $H_2$ evolution reactions**

The photocatalytic reactions were conducted in a top-irradiation vessel, which is connected to a glass-enclosed gas circulation system. A 300 W Xe-lamp (Perforct Light, PLS-SXE 300) with a 420 nm cutoff filter was used as a visible light source for photocatalytic $H_2$ evolution. 50 mg $MAPbI_3$ perovskite powders are added to the 15 mL aqueous perovskite saturated HI solution with $H_3PO_2$ as a stabilizer. Then, a certain amount of $H_2PtCl_6$ solution (calculated as Pt metal) was added to the solution. The temperature of the reaction system was maintained at 288 K by circulating cooling water. The $H_2$ evolved from the reaction was analyzed by gas chromatography (Tianmei, GC-7900) using Ar as the carrier gas.

**Calculation of the Solar-to-hydrogen energy conversion efficiency**

The photocatalytic HI splitting of the hybrid system was carried out under irradiation with a solar simulator (AM 1.5G 100 mW $cm^{-2}$, XES-40S2-CE). The solar HI splitting

efficiency, so-called solar-to-hydrogen conversion efficiency, is the ratio of solar light converted to break the chemical bonding of HI. It could be calculated by means of the standard redox potential of $I^-$ oxidation and the $H^+$ reduction potential. Our calculation for HI splitting efficiency is based on the amount of evolved hydrogen. The standard hydrogen reduction potential is 0 V (versus RHE), and the $I^-$ oxidation potential to $I_3^-$ is 0.53 V (versus RHE). Based on the Nernst equation and the required ion concentration of $H^+$ (7.969 mol $L^{-1}$), $I^-$ (5.1575 mol $L^{-1}$), $I_3^-$ ($9.96 \times 10^{-4}$ mol $L^{-1}$) in the current test solution, the Cell Potential of E ($2H^+ + 2e^- \rightarrow H_2$), E ($3I^- \rightarrow I_3^- + 2e^-$) are calculated as 0.056 V and 0.441 V versus NHE, respectively.

E ($2H^+ + 2e^- \rightarrow H_2$) = $0 - 0.059/2 \times \log(1/7.969^2)$ = 0.0532 V (versus NHE)

E ($3I^- \rightarrow I_3^- + 2e^-$) = $0.53 + 0.059/2 \times \log(9.96 \times 10^{-4}/5.1575^3)$ = 0.378 V (versus NHE)

Therefore, the total potential of HI splitting in our system was calculated as 0.378 V – 0.0532 V = 0.325 V. The STH for solar driven HI splitting was calculated by the following equation:

$$Solar\ HI\ splitting\ efficiency\ (\%) = \frac{the\ produced\ H_2\ (mol) \times 6.02 \times 10^{23} \times 2 \times 0.325\ (eV) \times 1.6 \times}{Psolar\ (W\ cm^{-2}) \times area\ (cm^{-2}) \times time\ (s)} \times 100\%$$

For instance, in the case of the Pt (2.0 wt %)/$MAPbI_3$ (CuI-0.26 M), 514 μmol of $H_2$ was evolved after 30 min of light irradiation at 100 mW $cm^{-2}$. The reaction temperature is 298 K. The light irradiation area was 3.4 $cm^2$, the solar HI splitting efficiency was calculated to be 5.25%.

## Characterizations

The as-prepared perovskite samples are characterized by X-ray power diffraction (XRD) on a Rigaku DH-2700BH powder diffractometer using Cu-Kα radiation at an operating voltage of 40 kV and a current of 30 mA, with a scan step of 2 ° $min^{-1}$. UV-vis diffuse reflectance spectra were recorded on a UV-vis spectrophotometer (Shimadzu UV-2600) equipped with an integrating sphere, using 100% $BaSO_4$ as reflectance standard. The morphology of perovskite was studied by scanning electron microscopy (SEM) with Regulus 8100. X-ray photoelectron spectroscopy (XPS) measurement was performed using a Thermo Fischer, ESCALAB 250Xi spectrometer with an Al Kα X-ray source. The amount of Cu species in perovskite samples were detected by inductively coupled plasma optical emission spectrometer (ICP-OES, Thermo Fisher Scientific ICAP 6000). Linear sweep voltammetry (LSV) was performed on a CHI660E electrochemical workstation using 0.5 M $Na_2SO_4$ and 0.5 M KI solution as the electrolyte in a three-electrode system. FTO or CuI/FTO film was employed as the working electrode, carbon sheet was employed as the counter electrode, and an Ag/AgCl was employed as the reference electrode. Steady-state photoluminescence (PL) spectra and time-resolved photoluminescence (TRPL) spectra was obtained on Edinburgh fluorescence spectrometer (FLS1000).

## Surface photovoltage microscopy (SPVM)

The topographic images of perovskite samples were measured using an autonomously built setup (Bruker Dimension V SPM system) with Pt/Ir coated tips (resonant

frequency 72 kHz). The surface potential is the difference in function between the perovskite sample surface and the Pt/Ir coated tip, tested using the AM-SPVM model with a scan rate of 0.5 HZ and tip lift height of 30 nm. A 500 W Xe lamp was used and modulated by a grating.

**TA set-up**

A beam of ultra-short pulse laser with a wavelength of 800 nm is emitted from the regeneratively amplified Ti: sapphire laser system (Coherent; 800 nm, 70 fs, 6 mJ/pulse, and 1 kHz repetition rate) in the ultra-fast femtosecond laser system, which is split into two laser beams after passing through a 1:9 beam splitter. The larger 90% of the laser beam in the transmitted part passes through the optical delay line ODL and is frequency doubled to 400 nm by a BBO crystal as the pump beam. The pump beam passes through the center of the convex lens and is focused on the sample to be tested at a certain angle. The sample is excited from the ground state to the excited state. The less powerful 10% of the reflected portion is partially attenuated with a neutral density filter and focused into a 2 mm thick sapphire window to generate a white light continuum used for probe beam. The probe beam passes through the center of the convex lens and is focused together with the pump beam at the same location on the sample. And ensure that the pump beam and the probe beam are spatially coincident (spatial coincidence refers to the coincidence of the spots of the two beams) and temporally (at time zero, the laser pulses of the two beams arrive at the same position of the sample at the same time). In this way, the sample molecules excited from the ground state to the excited state will absorb the probe beam in the excited state. After passing through the sample, the pump

beam incident on the sample at a certain angle will be blocked by the diaphragm and will not be received by the fiber probe, while the probe beam carrying the excited state information will be received by the fiber probe and then focused into fiber-coupled spectrometer with CMOS sensors with a detection frequency of 1 kHz. A variable neutral point control-density filter wheel was used to adjust the pump pulse intensity during the experiment. A synchronous chopper cuts off the pump pulse at 500 Hz and the absorbance change is calculated with two adjacent probe pulses.

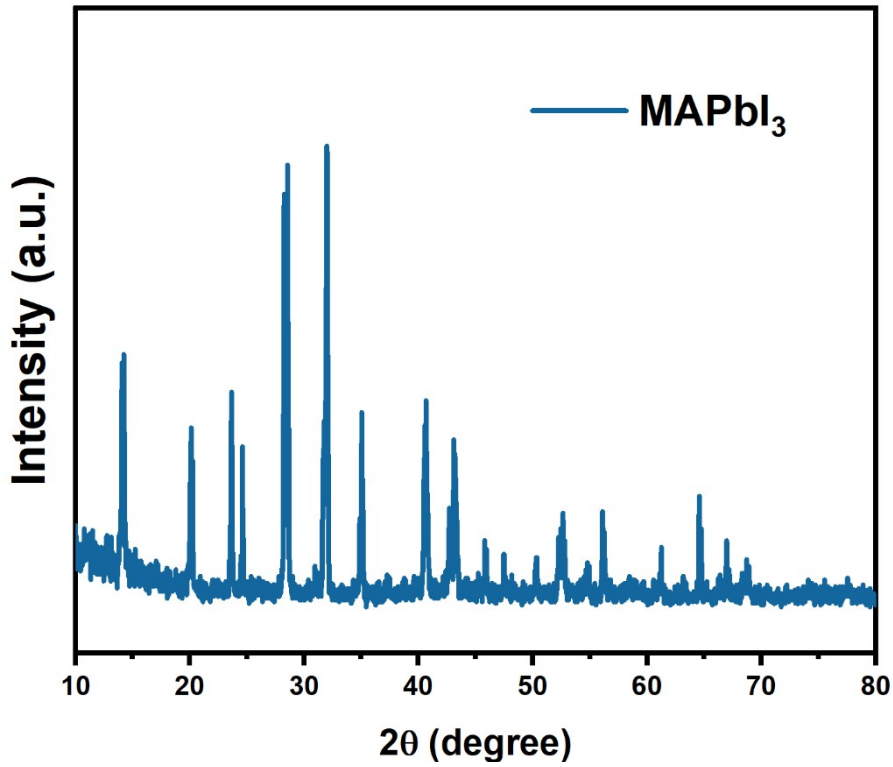


**Figure S1.** XRD pattern of the as-prepared $MAPbI_3$ powder.

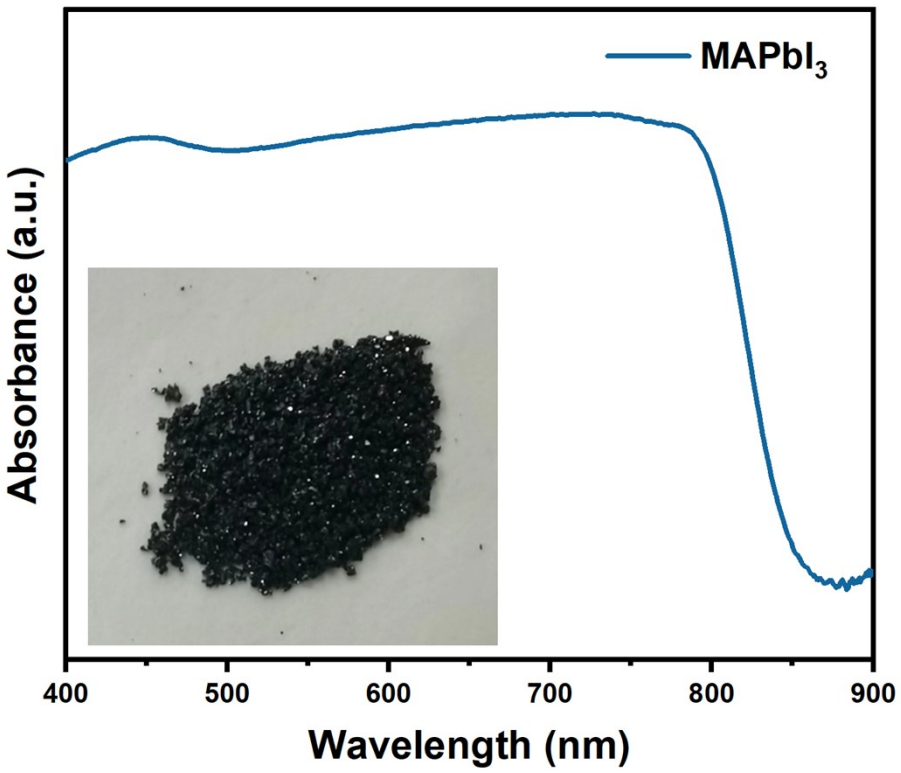


**Figure S2.** UV-vis diffuse reflectance spectrum of the $MAPbI_3$ powder. The inset shows the photograph of the $MAPbI_3$ powder.

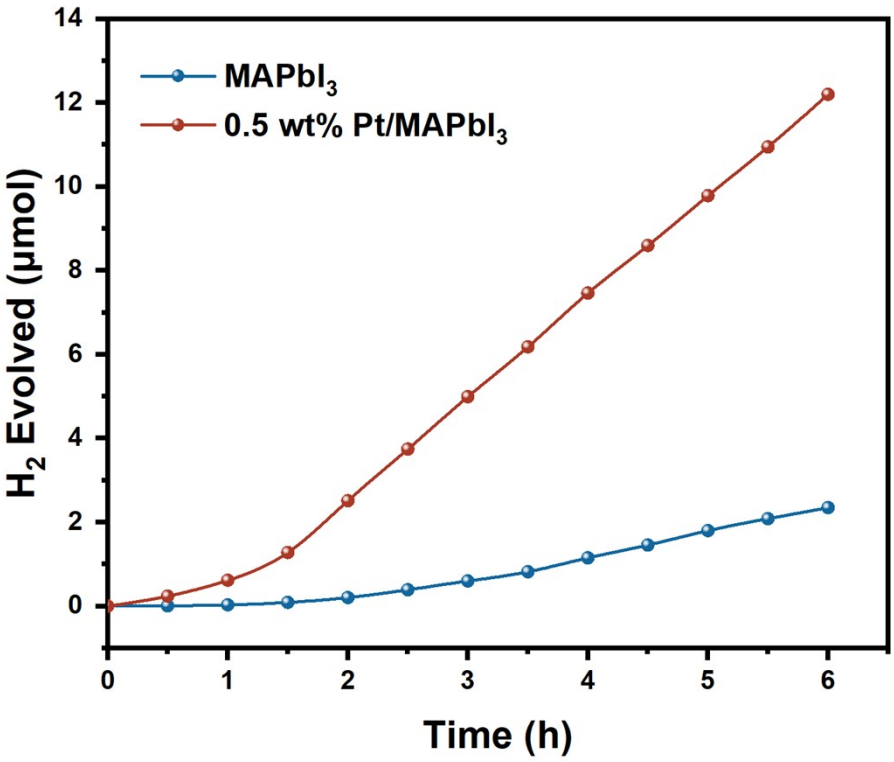


**Figure S3.** Time courses of photocatalytic $H_2$ evolution on $MAPbI_3$ and Pt (0.5 wt%)/$MAPbI_3$ in saturated HI solution. Reaction conditions: 15 mL perovskite saturated solutions, 50 mg of perovskite photocatalyst, 300 W xenon lamp ($\lambda$>420 nm), reaction cell: top-irradiation cell with a Pyrex window, reaction temperature: 288 K.

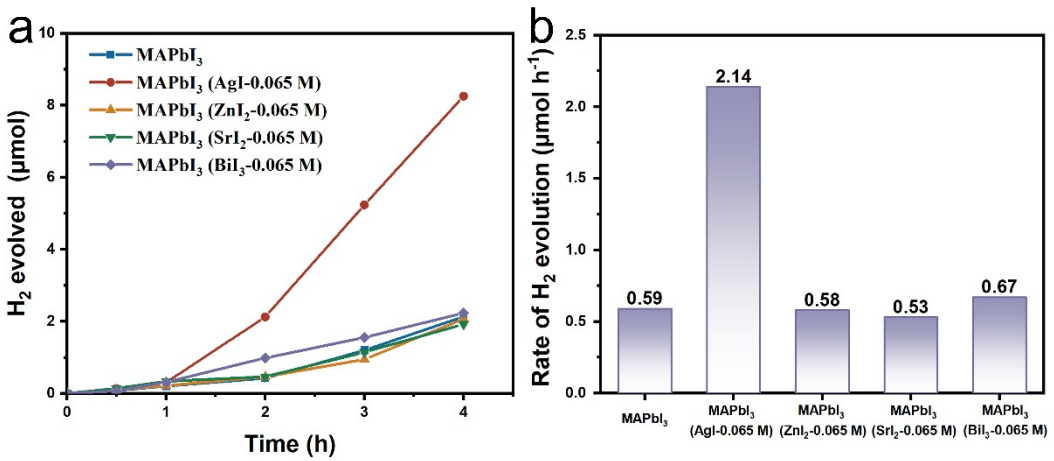


**Figure S4.** (a) Time courses of photocatalytic $H_2$ evolution in $MAPbI_3$, $MAPbI_3$ (AgI-0.065 M), $MAPbI_3$ ($ZnI_2$-0.065 M), $MAPbI_3$ ($SrI_2$-0.065 M) and $MAPbI_3$ ($BiI_3$-0.065 M) systems. (b) The rates of $H_2$ evolution in $MAPbI_3$, $MAPbI_3$ (AgI-0.065 M), $MAPbI_3$ ($ZnI_2$-0.065 M), $MAPbI_3$ ($SrI_2$-0.065 M) and $MAPbI_3$ ($BiI_3$-0.065 M) systems at stabilized stage. Reaction conditions: 15 mL perovskite saturated solutions, 50 mg of perovskite photocatalyst, 300 W xenon lamp ($\lambda$>420 nm), reaction cell: top-irradiation cell with a Pyrex window, reaction temperature: 288 K.

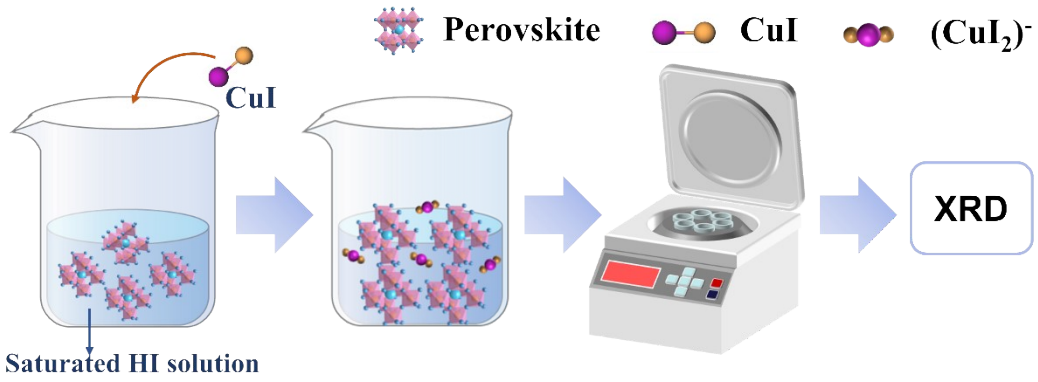


**Figure S5.** Schematic procedure of obtaining perovskite powder from the $MAPbI_3$ (CuI-x M) reaction system that has not been subjected to light irradiation.

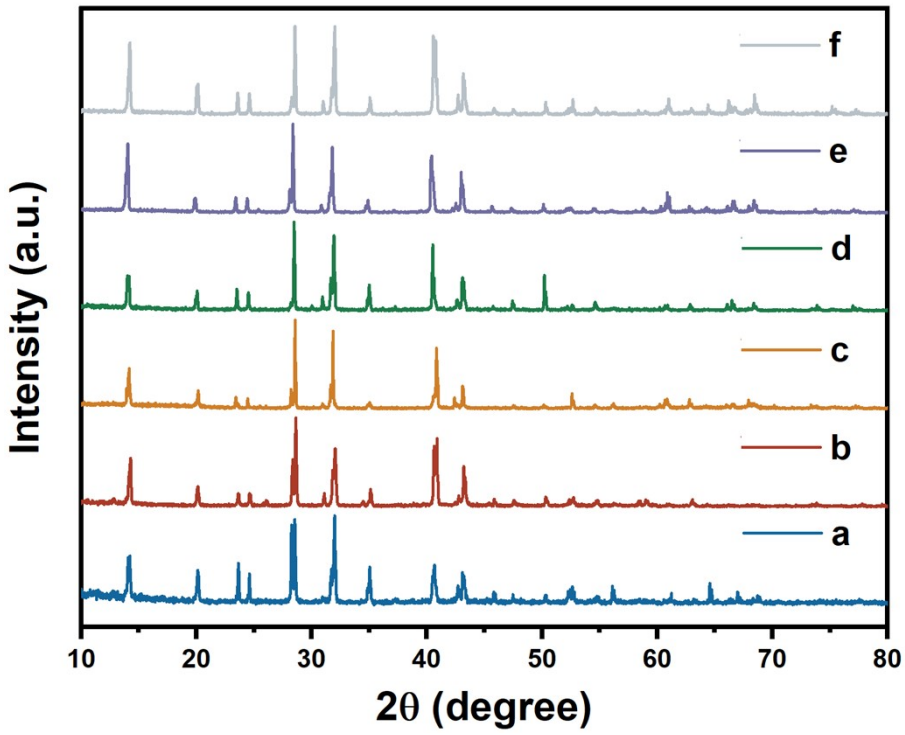


**Figure S6.** XRD patterns of the perovskite powder separated from the $MAPbI_3$ (CuI-x M) reaction system that has not been subjected to light irradiation. (a) x=0, (b) x=0.065, (c) x=0.13, (d) x=0.195, (e) x=0.26 and (f) x=0.325.

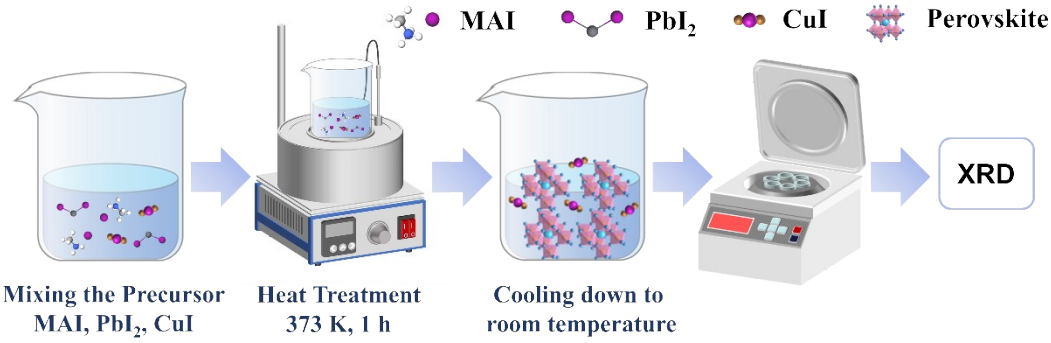


**Figure S7.** Schematic procedure of preparing perovskite powder by mixing MAI, $PbI_2$ and different amounts of CuI in the synthesis solution.

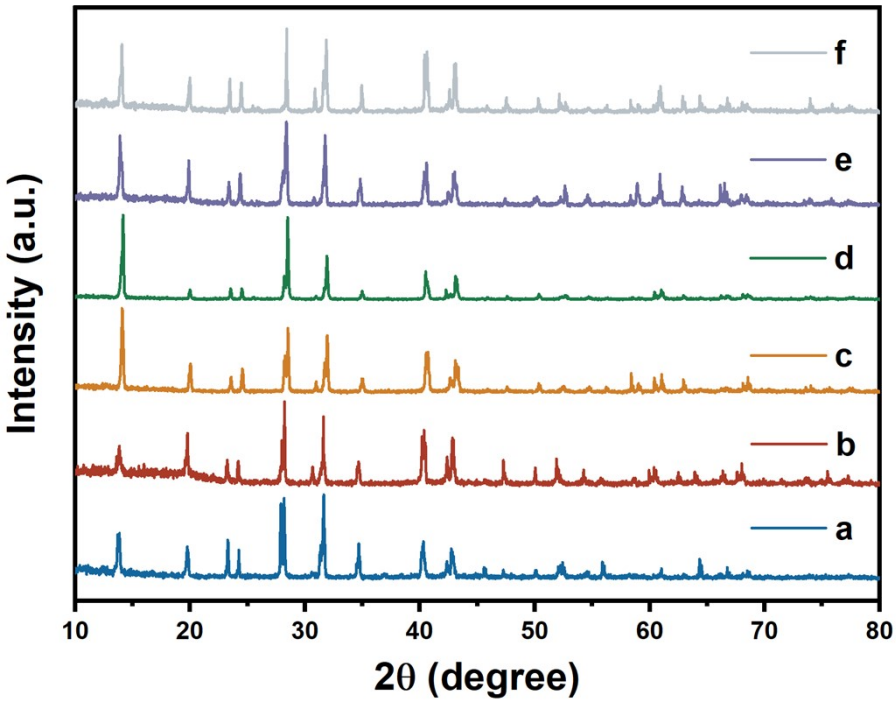


**Figure S8.** XRD patterns of the powder obtained with the synthesis procedure shown in **Figure S6**. (a) x=0, (b) x=0.065, (c) x=0.13, (d) x=0.195, (e) x=0.26 and (f) x=0.325.

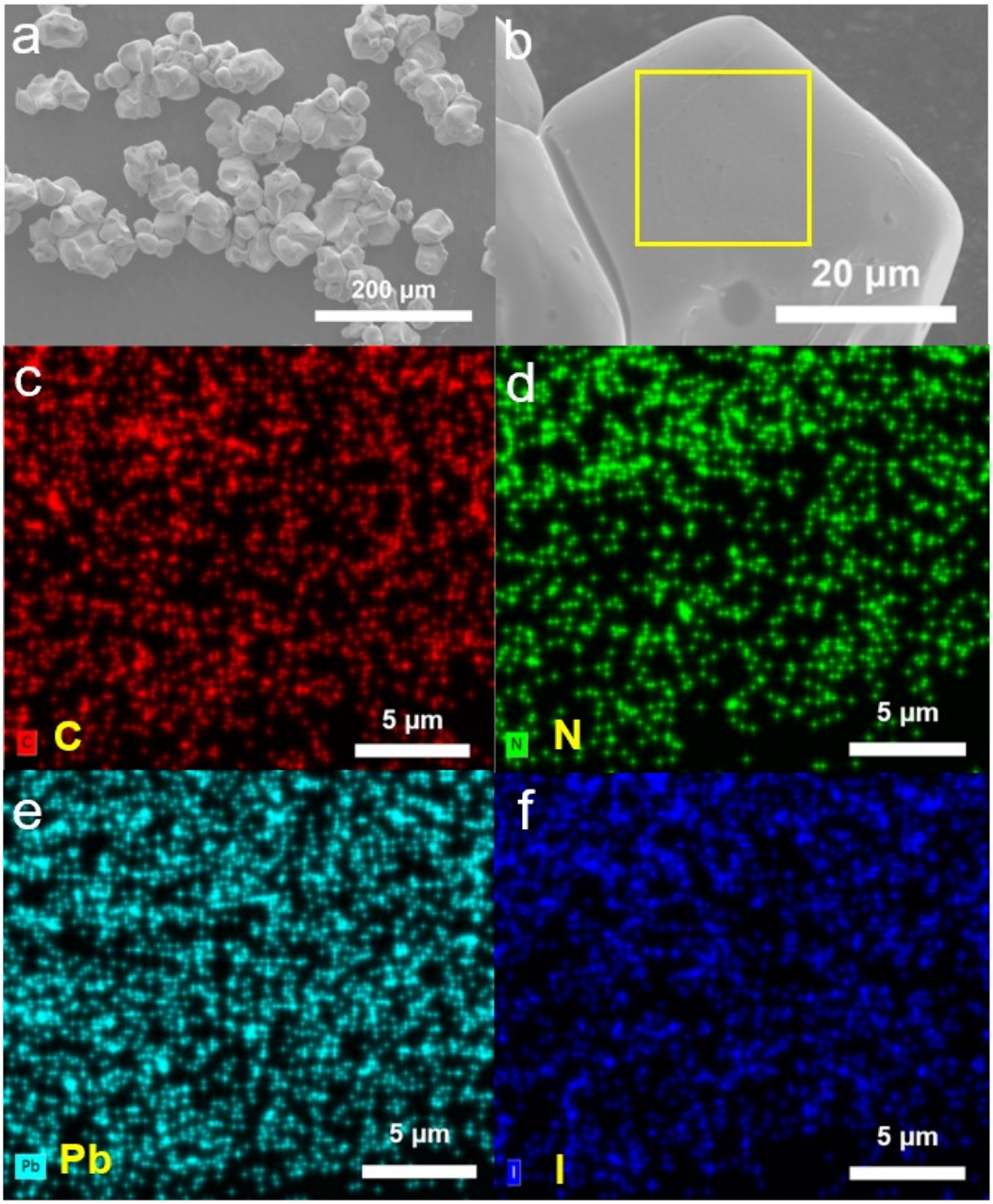


**Figure S9.** (a)-(b) SEM images of pure $MAPbI_3$. (b)-(f) The corresponding EDS mapping images of C, Pb, N and I elements of $MAPbI_3$.

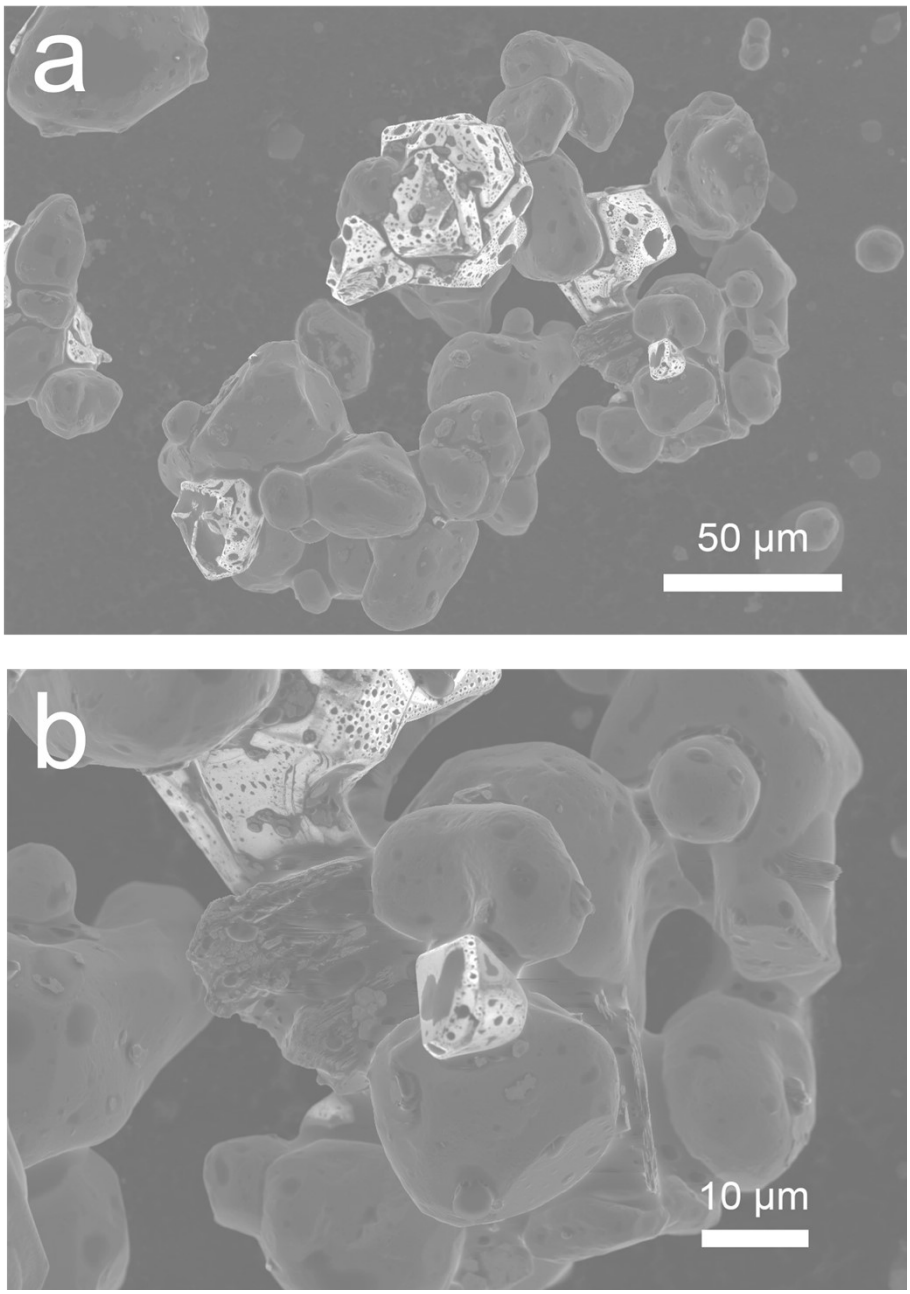


**Figure S10.** (a)-(b) SEM images of Powder-$MAPbI_3$ (CuI-0.26 M).

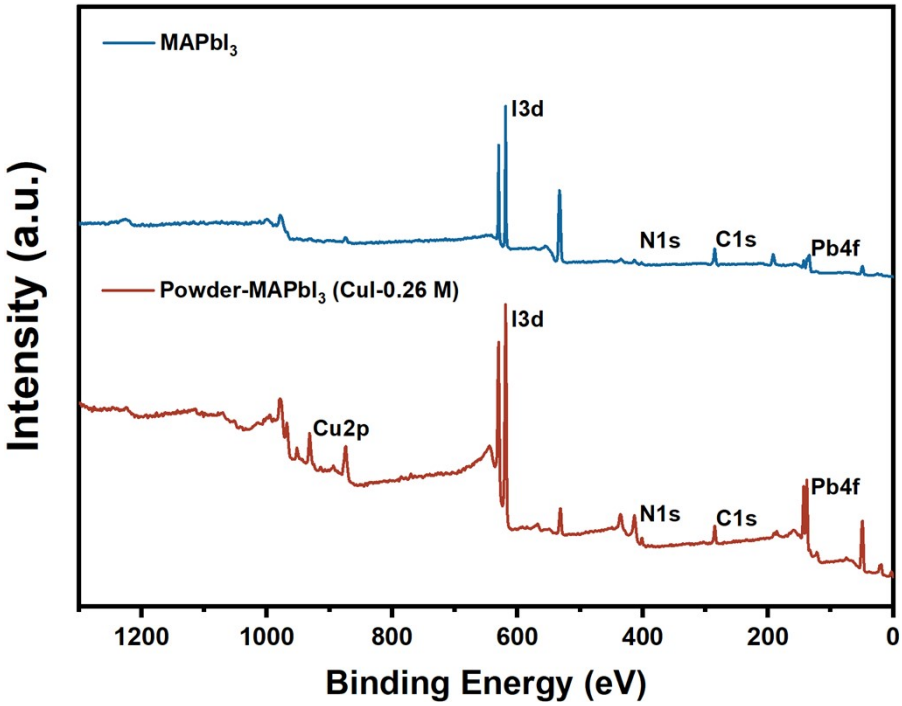


**Figure S11.** XPS survey spectra of $MAPbI_3$ and Powder-$MAPbI_3$ (CuI-0.26 M).

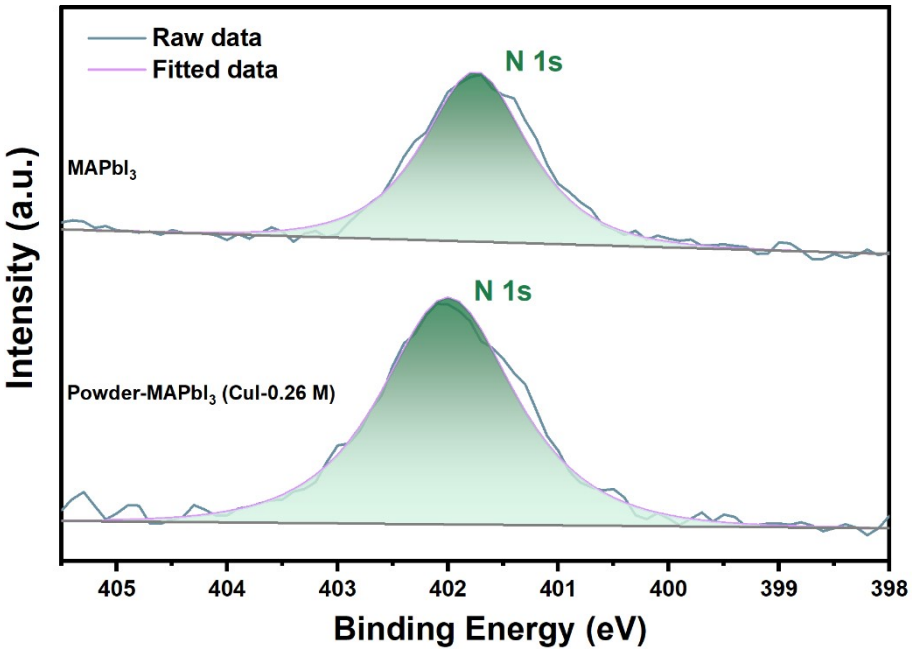


**Figure S12.** XPS spectra of N 1s of $MAPbI_3$ and Powder-$MAPbI_3$ (CuI-0.26 M).

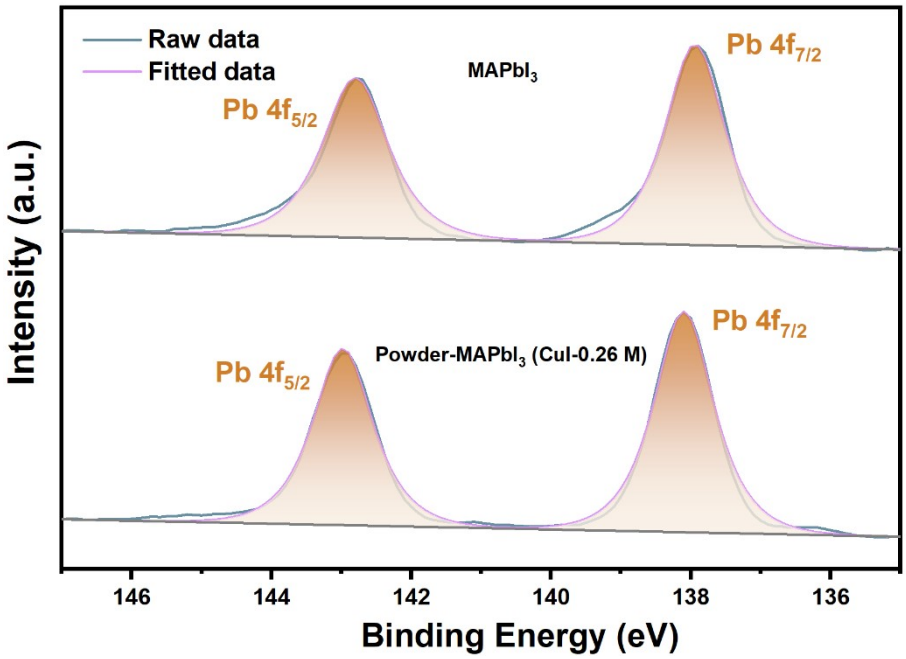


**Figure S13.** XPS spectra of Pb 4f of $MAPbI_3$ and Powder-$MAPbI_3$ (CuI-0.26 M).

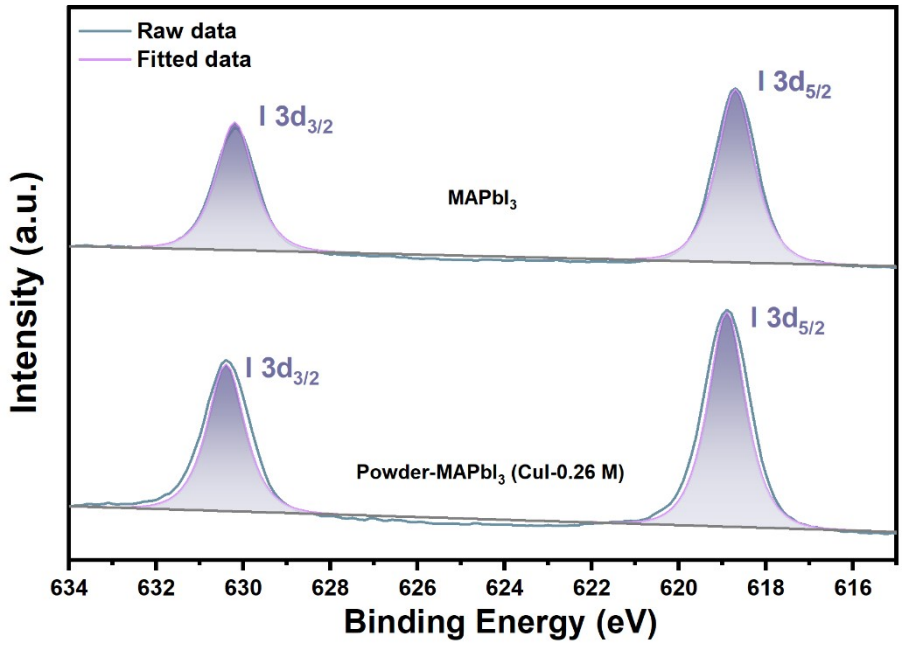


**Figure S14.** XPS spectra of I3d of $MAPbI_3$ and Powder-$MAPbI_3$ (CuI-0.26 M).

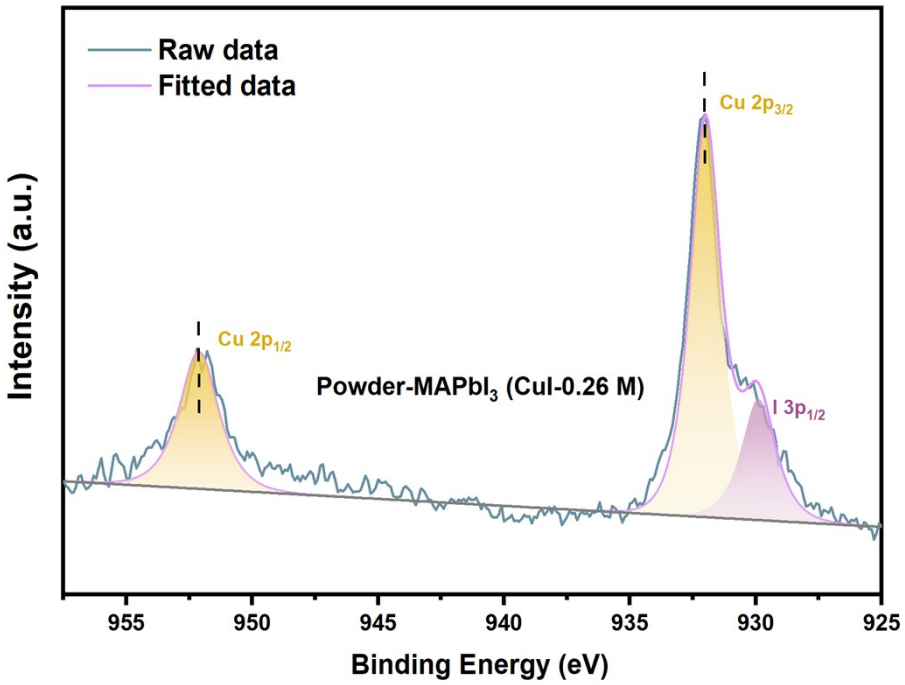


**Figure S15.** XPS spectrum of Cu 2p of Powder-$MAPbI_3$ (CuI-0.26 M). The peak at *ca.* 930.0 eV is ascribed to I $3p^{1-3}$.

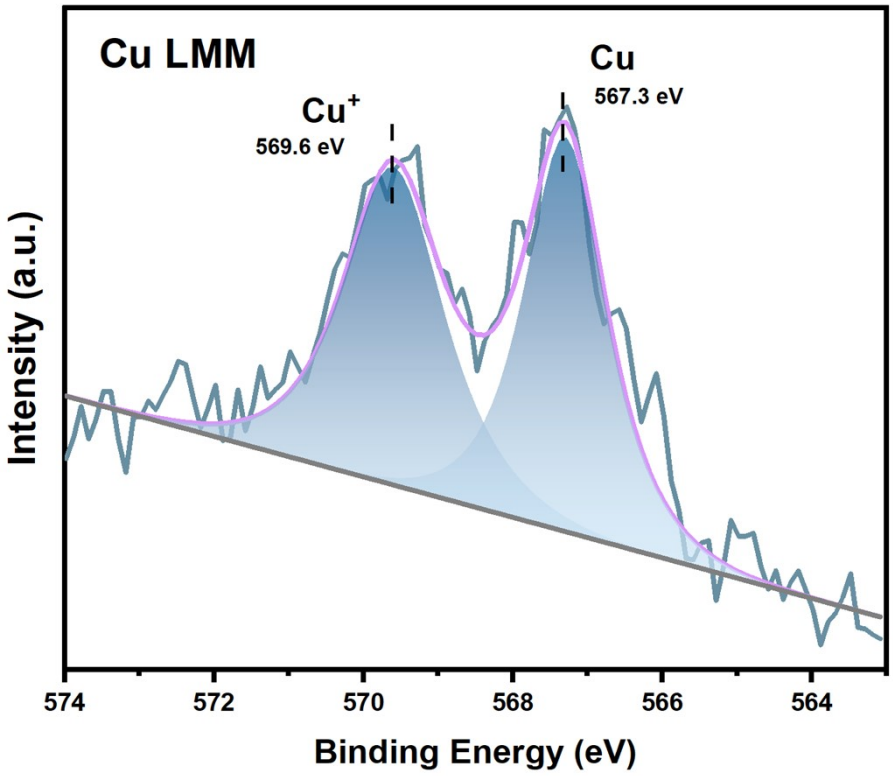


**Figure S16.** Cu LMM spectrum of Powder-$MAPbI_3$ (CuI-0.26 M).

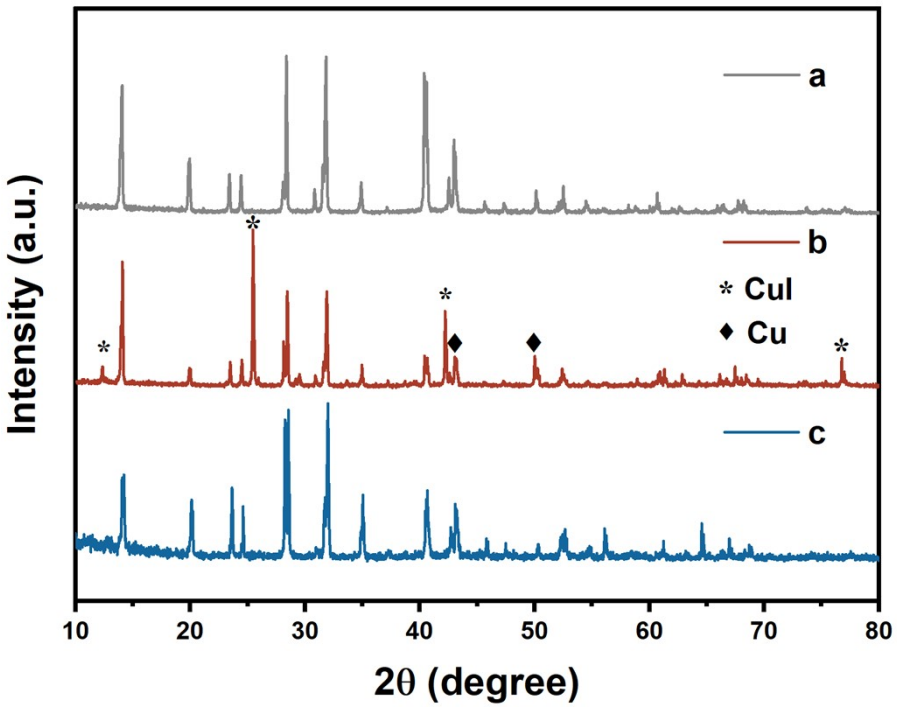


**Figure S17.** XRD patterns of (a) the sample separated from the $MAPbI_3$ (CuI-0.26 M) system that is kept under off-light conditions for 7 days after the photocatalytic reaction has been stopped, (b) Powder-$MAPbI_3$ (CuI-0.26 M) and (c) $MAPbI_3$.

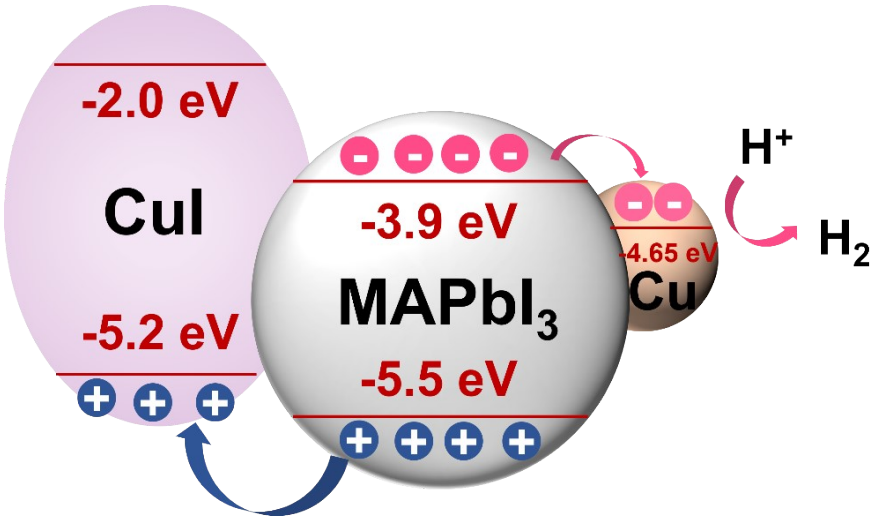


**Figure S18.** Schematic energy-level diagrams of $MAPbI_3$[4], CuI[5] and metallic Cu.

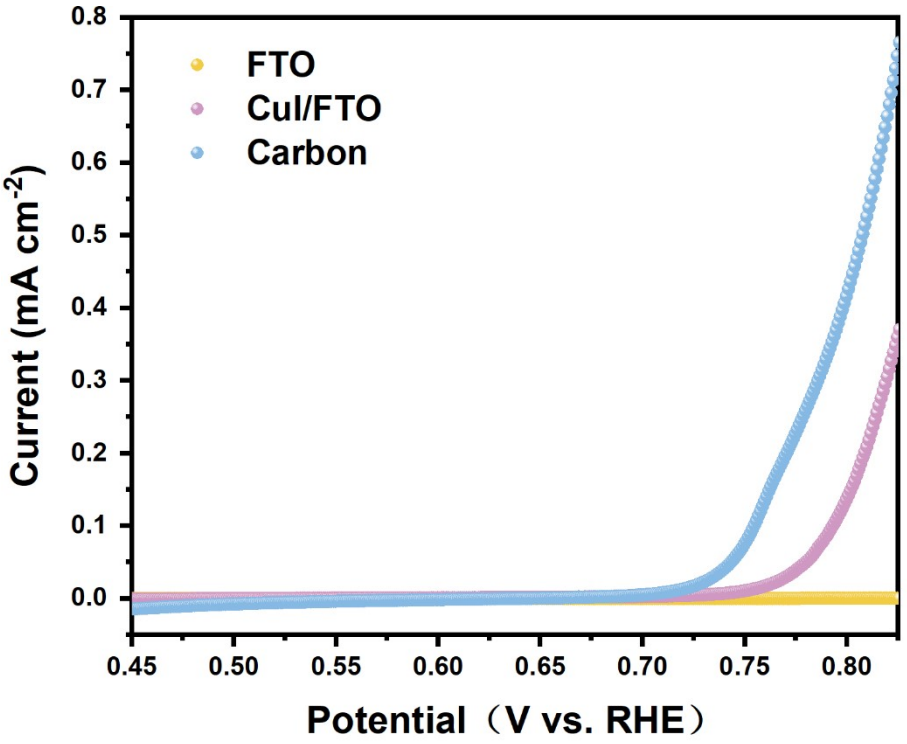


**Figure S19.** Linear sweep voltammetry curves of CuI/FTO, carbon and FTO electrodes for $I^-$ oxidation reaction in 0.5 M $Na_2SO_4$ and 0.5 M KI electrolyte.

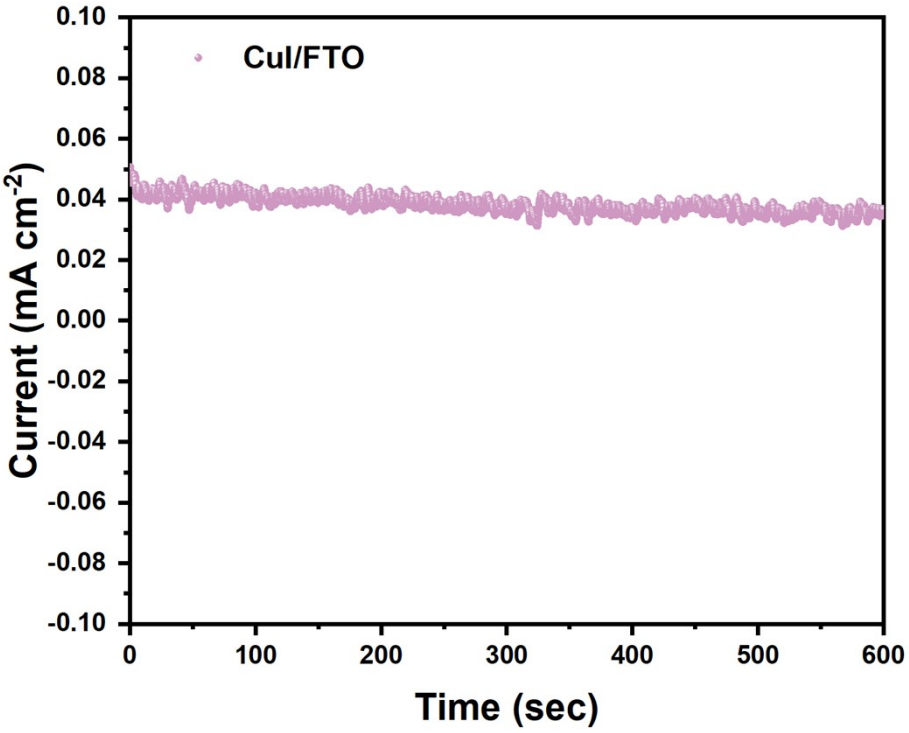


**Figure S20.** Chronoamperometry test of CuI/FTO electrode for the $I^-$ oxidation reaction in 0.5 M $Na_2SO_4$ and 0.5 M KI electrolyte at an applied potential of 0.779 V vs. RHE.

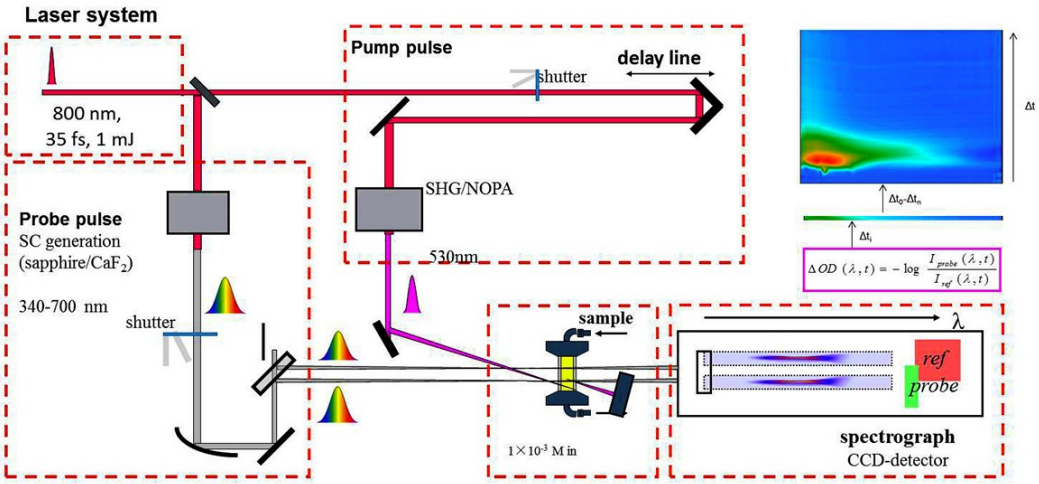


**Figure S21.** Schematic of the transient absorption setup with laser system and transient spectrometer.

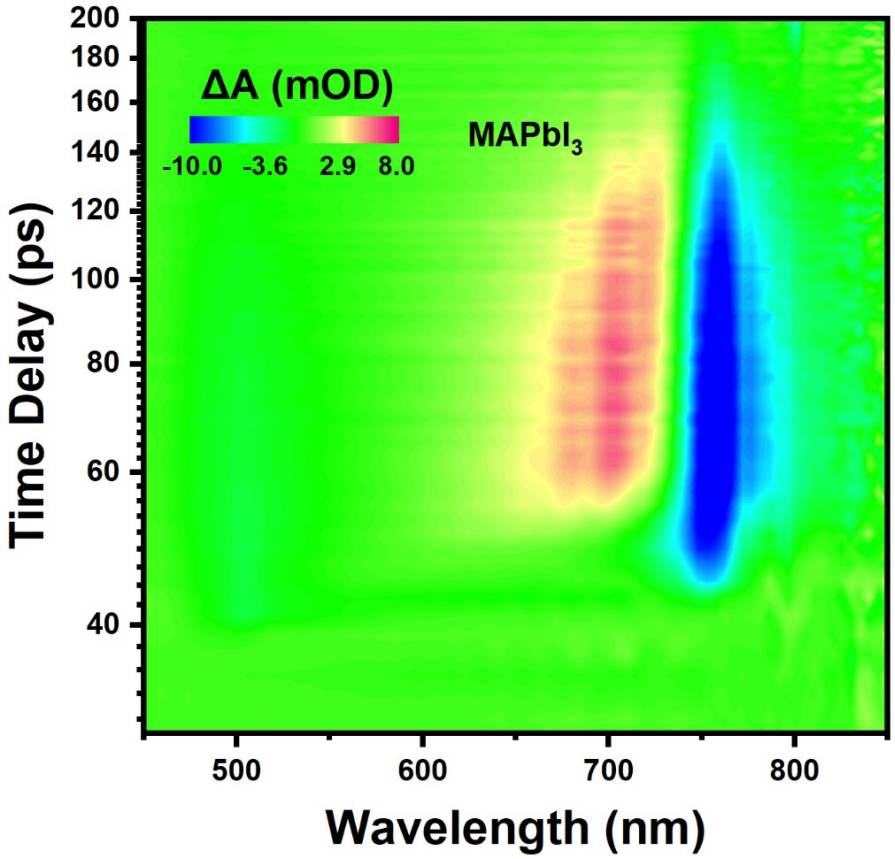


**Figure S22**. Two-dimensional pseudo color plots of TA spectra of $MAPbI_3$ at 400 nm excitation.

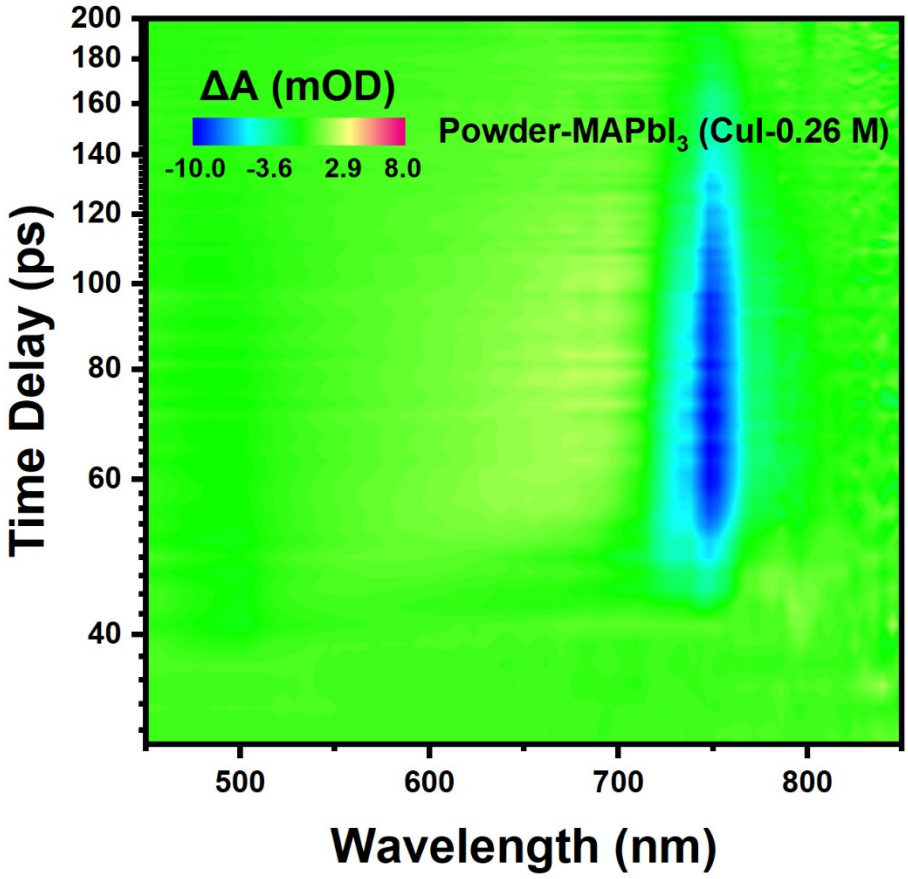


**Figure S23**. Two-dimensional pseudo color plots of TA spectra of Powder-$MAPbI_3$ (CuI-0.26 M) at 400 nm excitation.

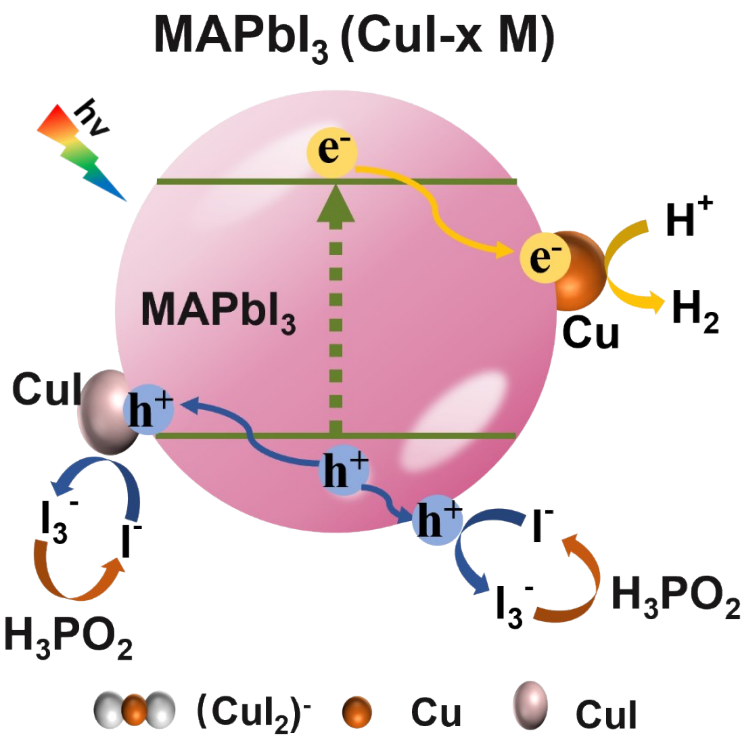


**Figure S24**. Schematic illustration of the mechanism of the photocatalytic $H_2$ evolution in the $MAPbI_3$ (CuI-0.26 M) system.

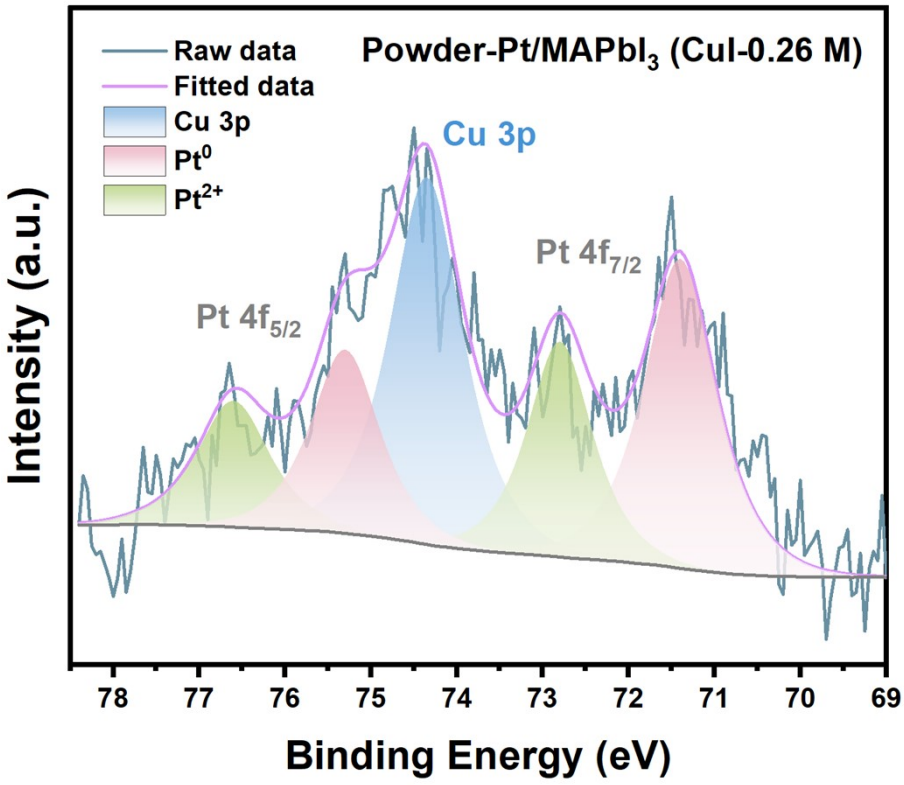


**Figure S25.** XPS spectrum of Pt 4f of Powder-Pt (2.0 wt%)/$MAPbI_3$ (CuI-0.26 M). The peak at 74.4 eV is assigned to the Cu 3p.

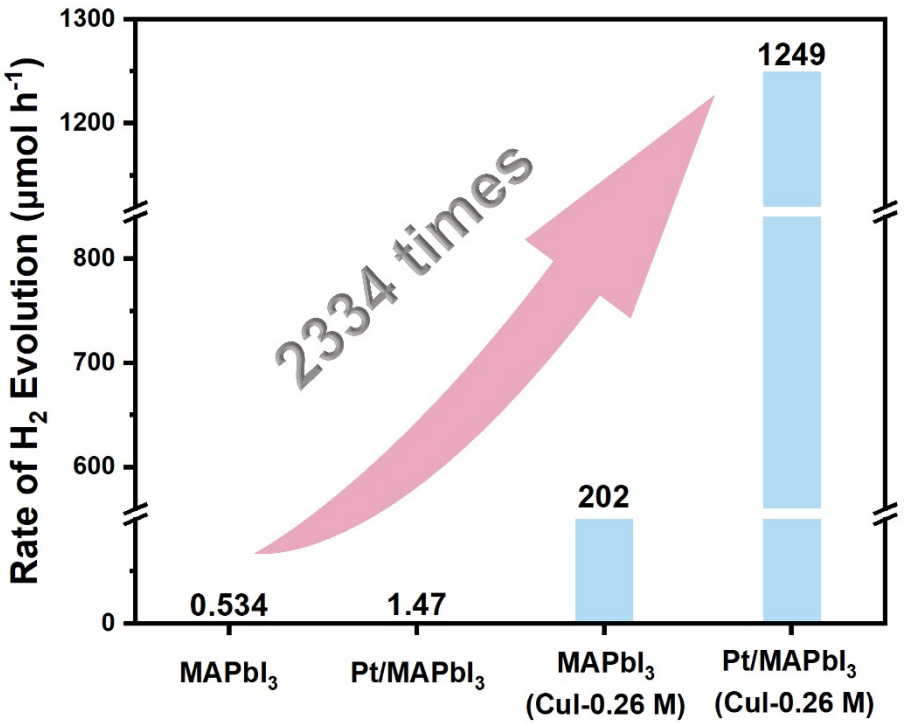


**Figure S26.** The rates of $H_2$ evolution on $MAPbI_3$, Pt (2.0 wt%)/$MAPbI_3$, $MAPbI_3$ (CuI-0.26 M) and Pt (2.0 wt%)/$MAPbI_3$ (CuI-0.26 M) system. Reaction conditions: 15 mL perovskite saturated solutions, 50 mg of perovskite photocatalyst, 300 W xenon lamp ($\lambda$>420 nm), reaction cell: top-irradiation cell with a Pyrex window, reaction temperature: 288 K.

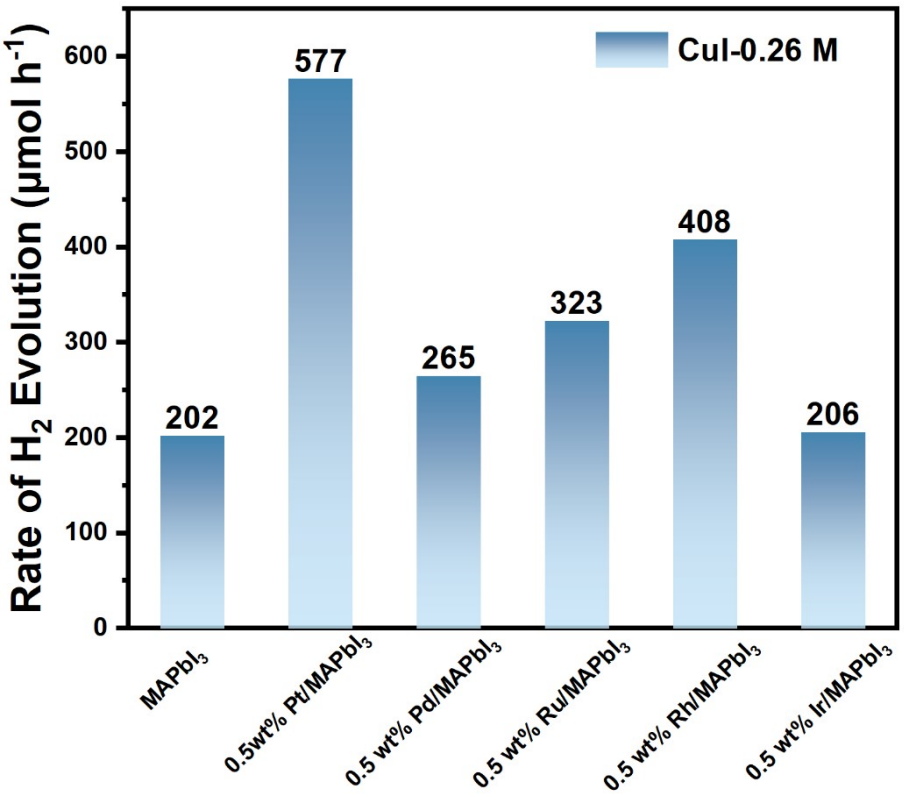


**Figure S27.** The rates of $H_2$ evolution in Pt (0.5 wt%)/$MAPbI_3$ (CuI-0.26 M), Pd (0.5 wt%)/$MAPbI_3$ (CuI-0.26 M), Ru (0.5 wt%)/$MAPbI_3$ (CuI-0.26 M), Rh (0.5 wt%)/$MAPbI_3$ (CuI-0.26 M) and Ir (0.5 wt%)/$MAPbI_3$ (CuI-0.26 M) systems. Reaction conditions: 15 mL perovskite saturated solutions, 50 mg of perovskite photocatalyst, 300 W xenon lamp ($\lambda$>420 nm), reaction cell: top-irradiation cell with a Pyrex window, reaction temperature: 288 K.

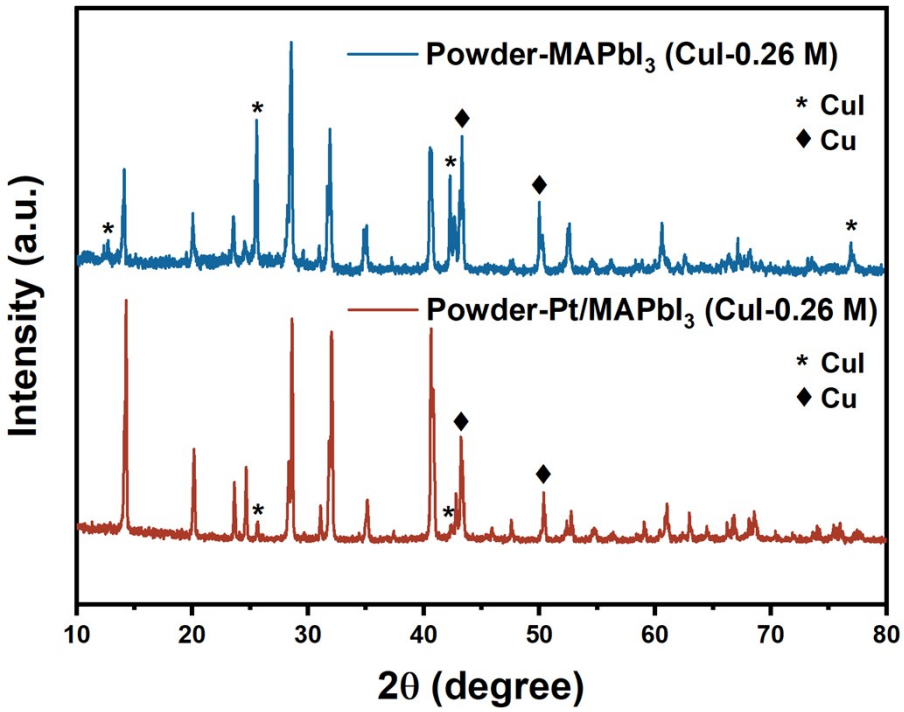


**Figure S28.** XRD patterns of Powder-$MAPbI_3$ (CuI-0.26 M) and Powder-Pt (2.0 wt%)/$MAPbI_3$ (CuI-0.26 M) after photocatalytic recycling tests.

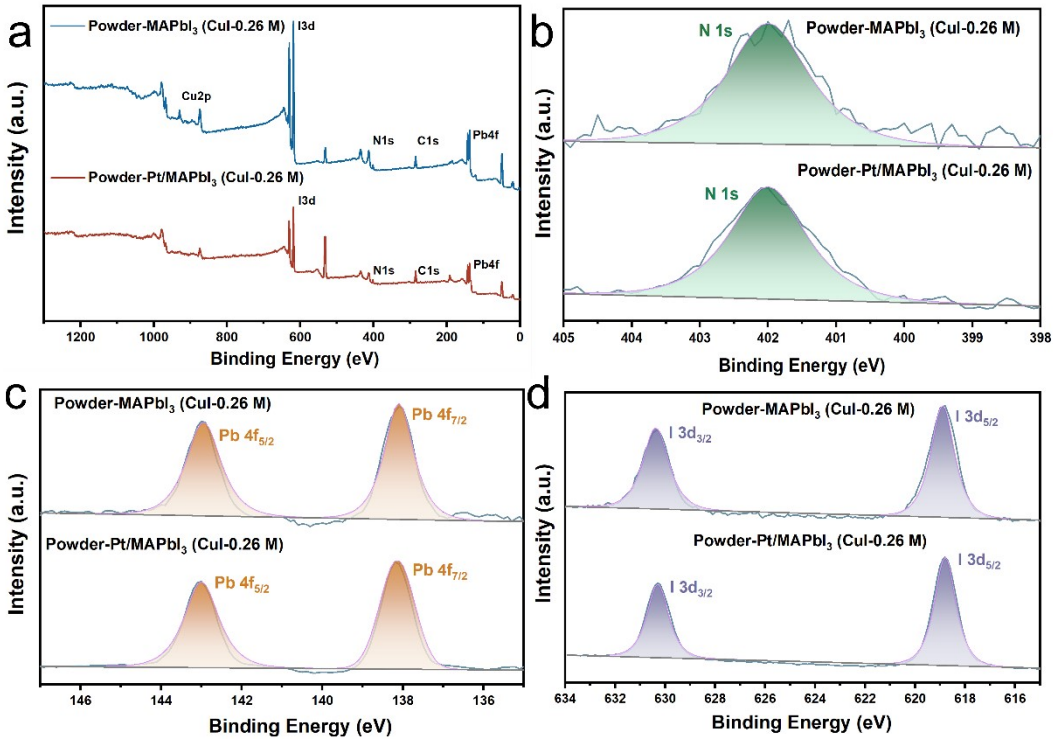


**Figure S29.** XPS spectra of Powder-$MAPbI_3$ (CuI-0.26 M) and Powder-Pt (2.0 wt%)/$MAPbI_3$ (CuI-0.26 M) after photocatalytic recycling tests. (a) XPS survey spectra, (b) N 1s, (c) Pb 4f and (d) I 3d regions.

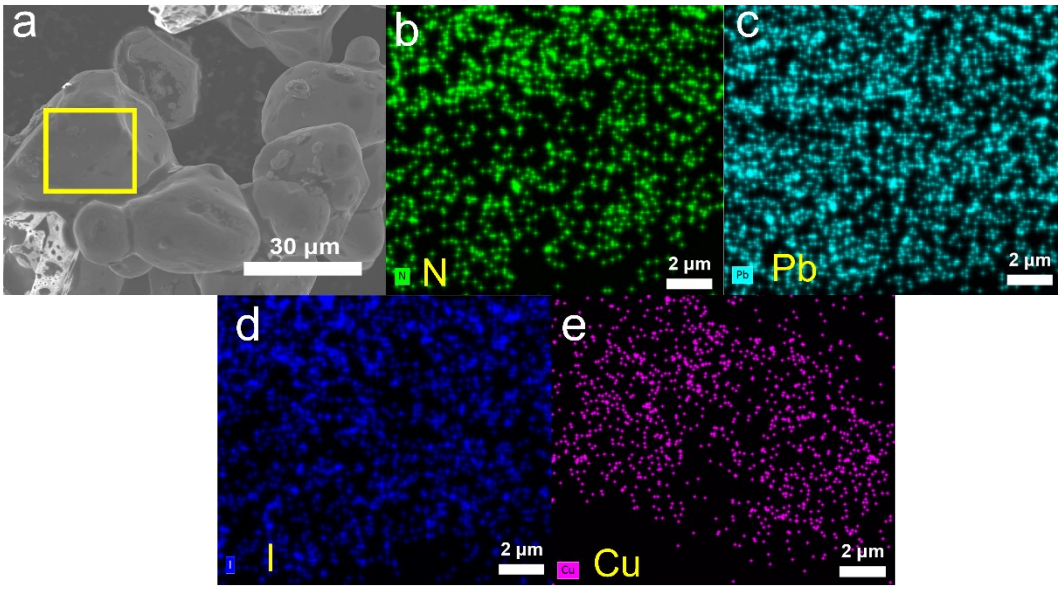


**Figure S30.** (a) SEM image of Powder-$MAPbI_3$ (CuI-0.26 M) after photocatalytic recycling tests. (b)-(e) The corresponding EDS mapping images of N, Pb, I and Cu elements of Powder-$MAPbI_3$ (CuI-0.26 M).

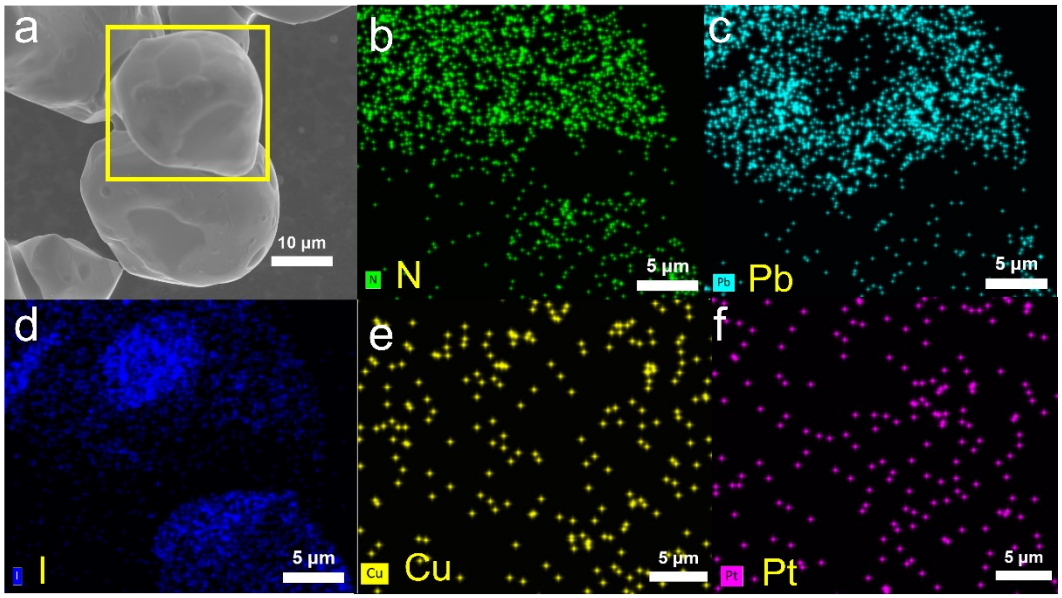


**Figure S31.** (a) SEM image of Powder-Pt (2.0 wt%)/$MAPbI_3$ (CuI-0.26 M) after photocatalytic recycling tests. (b)-(f) The corresponding EDS mapping images of N, Pb, I, Cu and Pt elements of Powder-Pt (2.0 wt%)/$MAPbI_3$ (CuI-0.26 M).

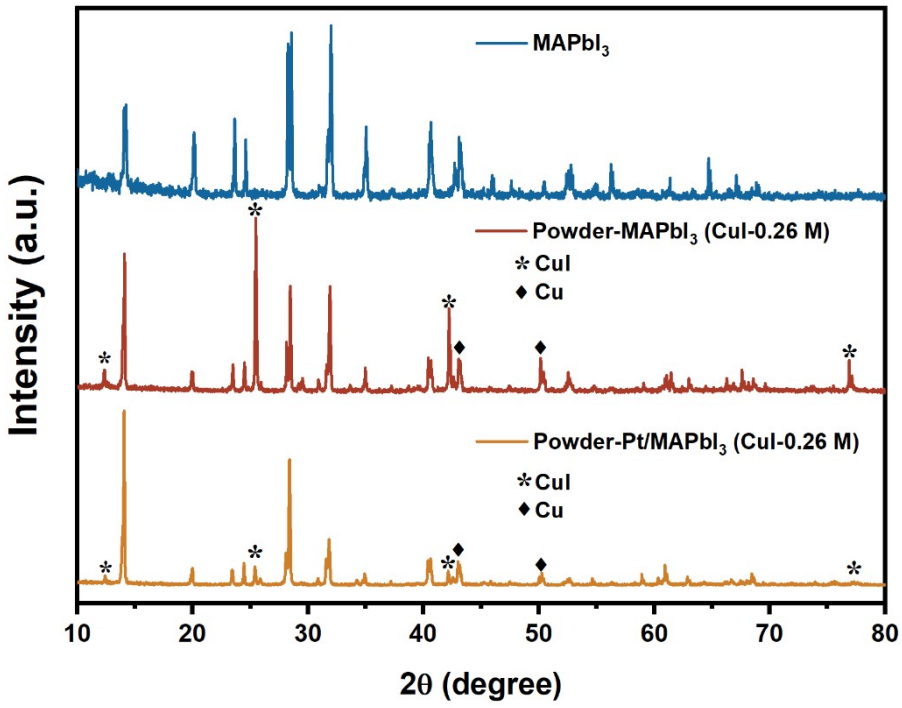


**Figure S32.** XRD patterns of $MAPbI_3$, Powder-$MAPbI_3$ (CuI-0.26 M) and Powder-Pt/$MAPbI_3$ (CuI-0.26 M).

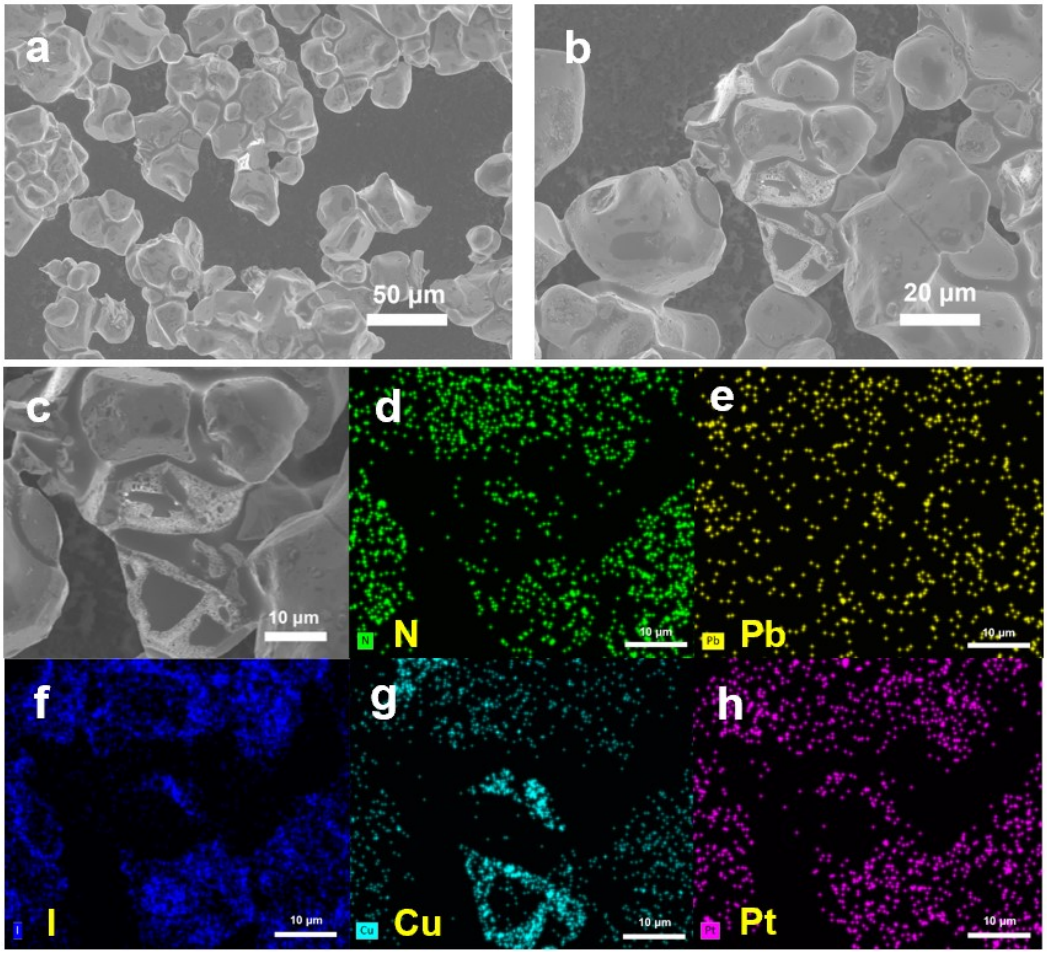


**Figure S33.** (a)-(b) SEM images of Powder-Pt (0.5 wt%)/$MAPbI_3$ (CuI-0.26 M). (c)-(h) The corresponding EDS elemental mapping of N, Pb, I, Cu and Pt of Powder-Pt (0.5 wt%)/$MAPbI_3$ (CuI-0.26 M).

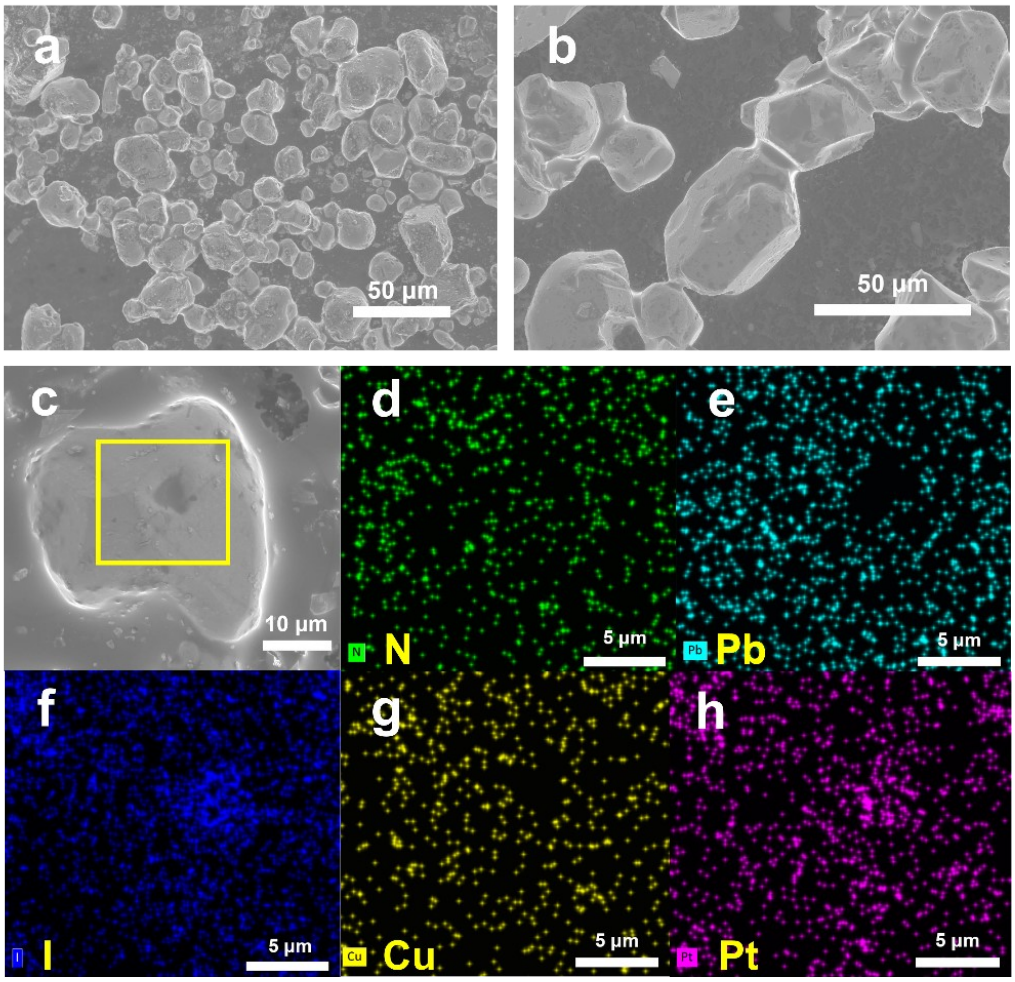


**Figure S34.** (a)-(b) SEM images of the Powder-Pt (2.0 wt%)/$MAPbI_3$ (CuI-0.26 M). (c)-(h) The corresponding EDS elemental mapping of N, Pb, I, Cu and Pt of Powder-Pt (2.0 wt%)/$MAPbI_3$ (CuI-0.26 M).

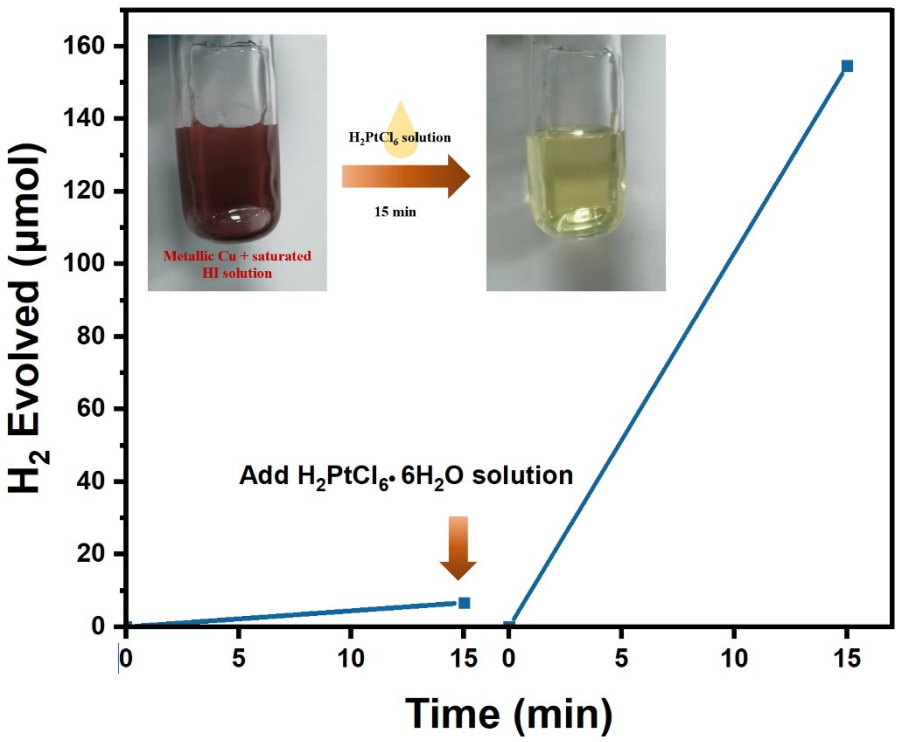


**Figure S35.** Influence of the $H_2PtCl_6 \cdot 6H_2O$ addition on the rate of $H_2$ evolution from saturated HI solution containing 0.26 M CuI and metallic Cu powder without light irradiation. Reaction conditions: 15 mL perovskite saturated solutions containing 0.26 M CuI and 20 mg of metallic Cu, reaction cell: a home-made reactor, reaction temperature: 288 K. The inset is the picture of the reaction solution containing metallic Cu (left) and that kept for 15 minutes after introducing $H_2PtCl_6 \cdot 6H_2O$ solution (right).

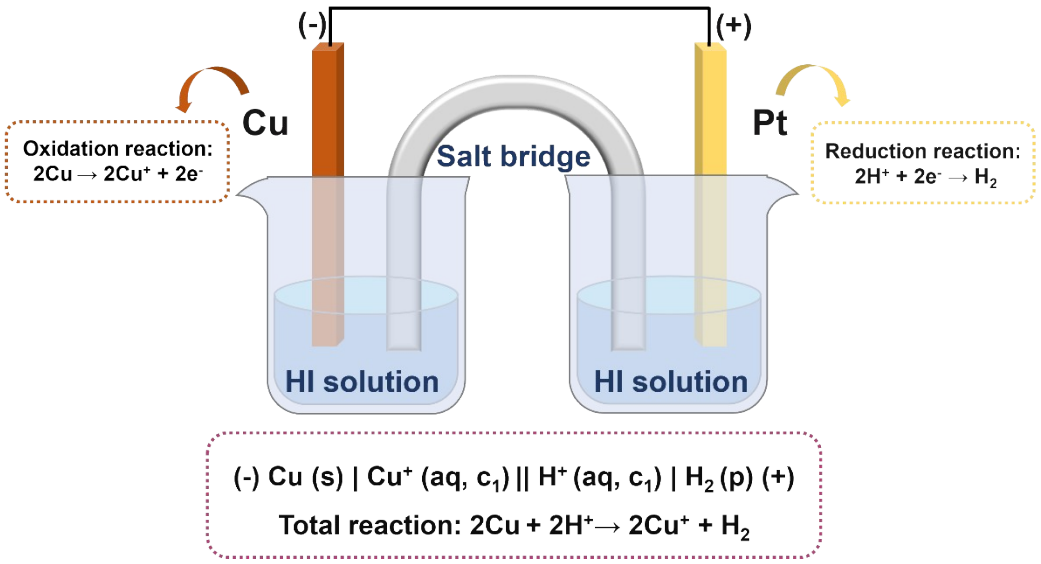


**Figure S36.** Schematic illustration of the electrochemical cell composed of metallic Cu and Pt electrodes in HI solution.

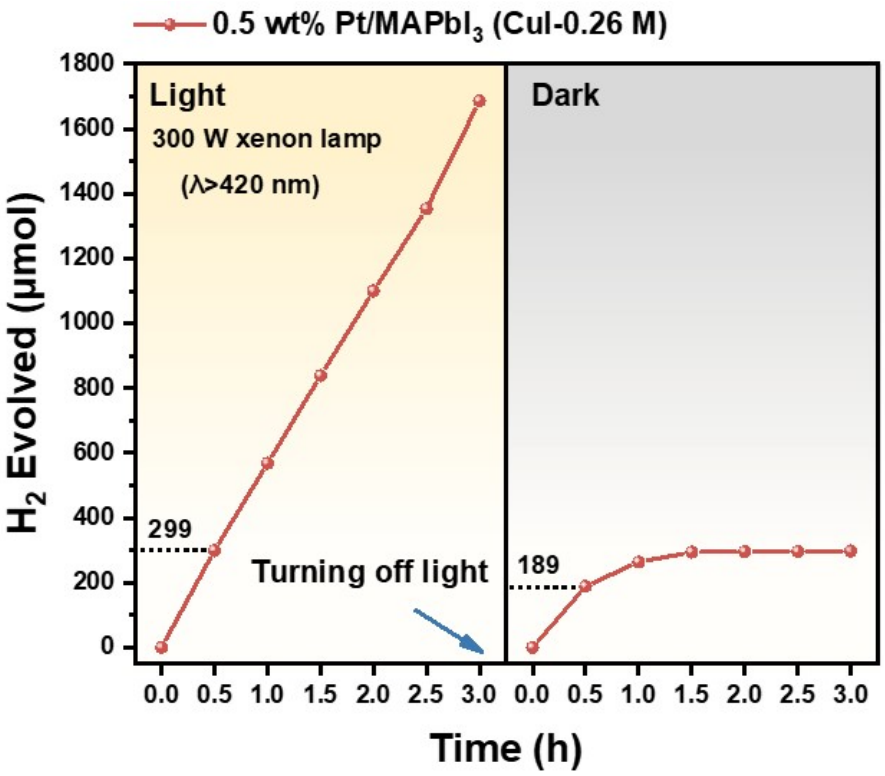


**Figure S37.** Time courses of $H_2$ released from the Pt (0.5 wt%)/$MAPbI_3$ (CuI-0.26 M) system after light irradiation is turned off. Reaction conditions: 15 mL perovskite saturated solutions, 50 mg of perovskite photocatalyst, reaction cell: top-irradiation cell with a Pyrex window, reaction temperature: 288 K.

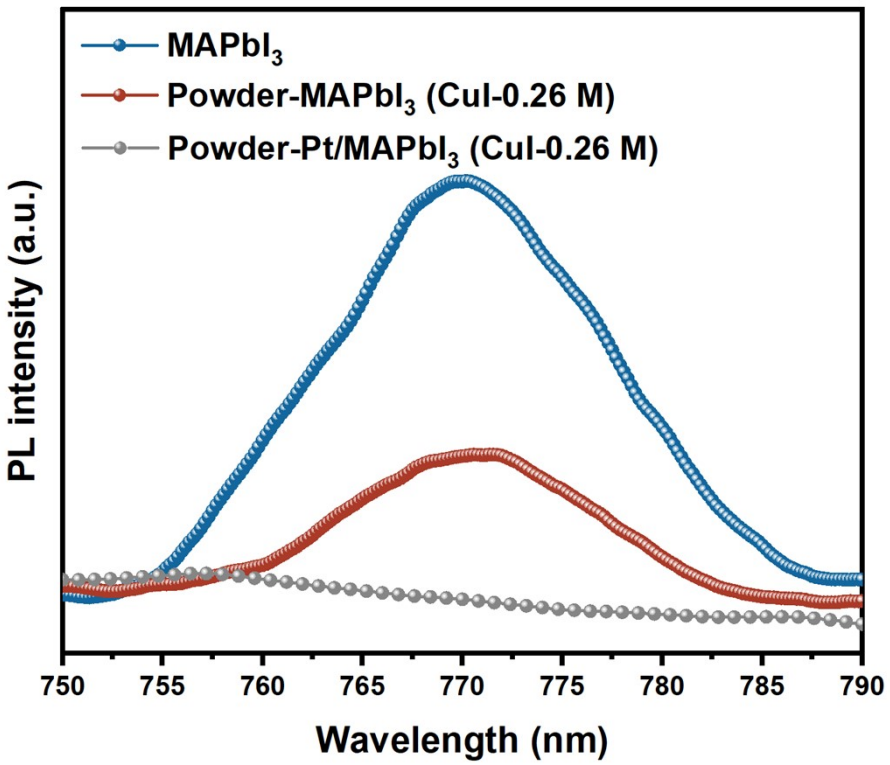


**Figure S38.** The PL spectra of $MAPbI_3$, Powder-$MAPbI_3$ (CuI-0.26 M) and Powder-Pt (2.0 wt%)/$MAPbI_3$ (CuI-0.26 M).

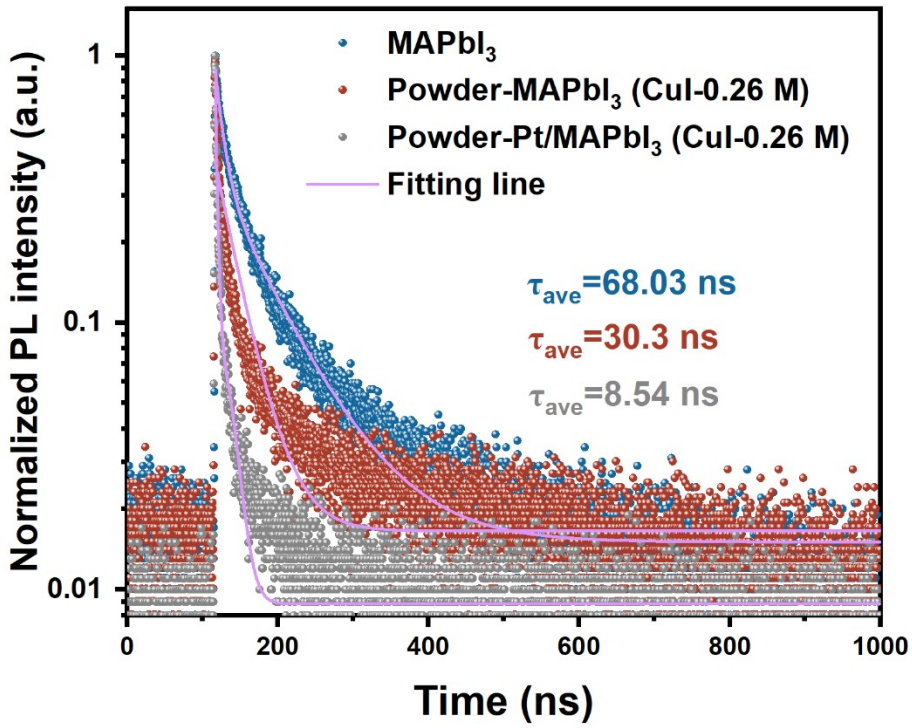


**Figure S39.** The TRPL decay curves of $MAPbI_3$, Powder-$MAPbI_3$ (CuI-0.26 M) and Powder-Pt (2.0 wt%)/$MAPbI_3$ (CuI-0.26 M).

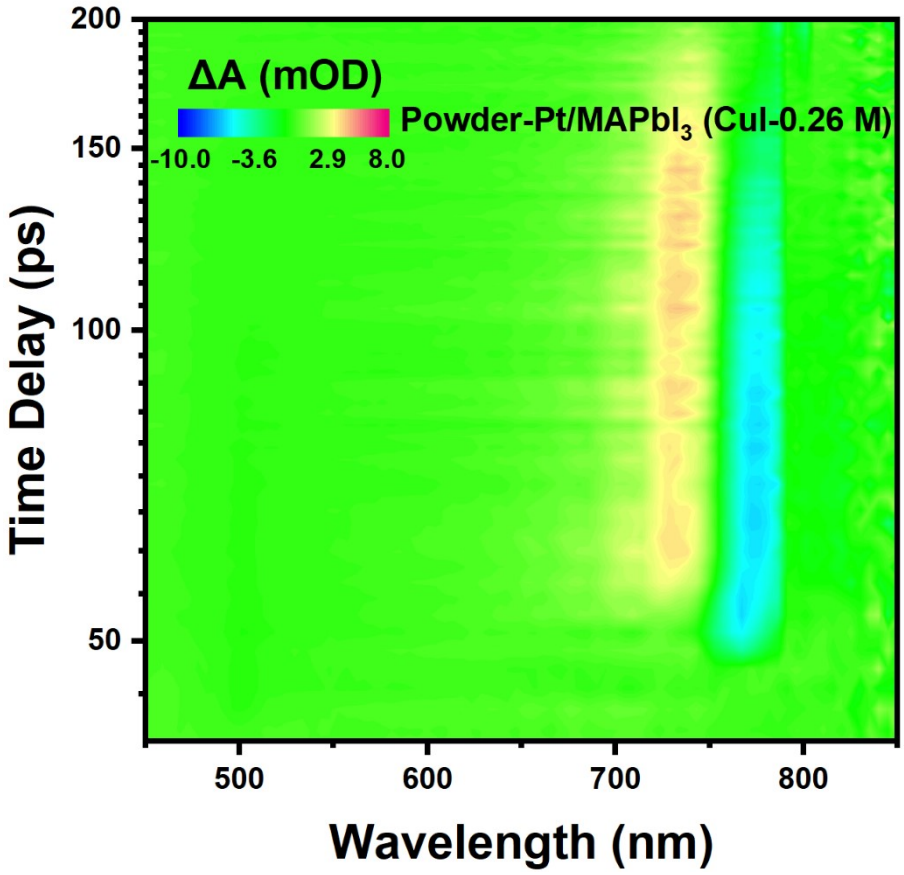


**Figure S40**. Two-dimensional pseudo color plots of TA spectra of Powder-Pt (2.0 wt%)/$MAPbI_3$ (CuI-0.26 M) at 400 nm excitation.

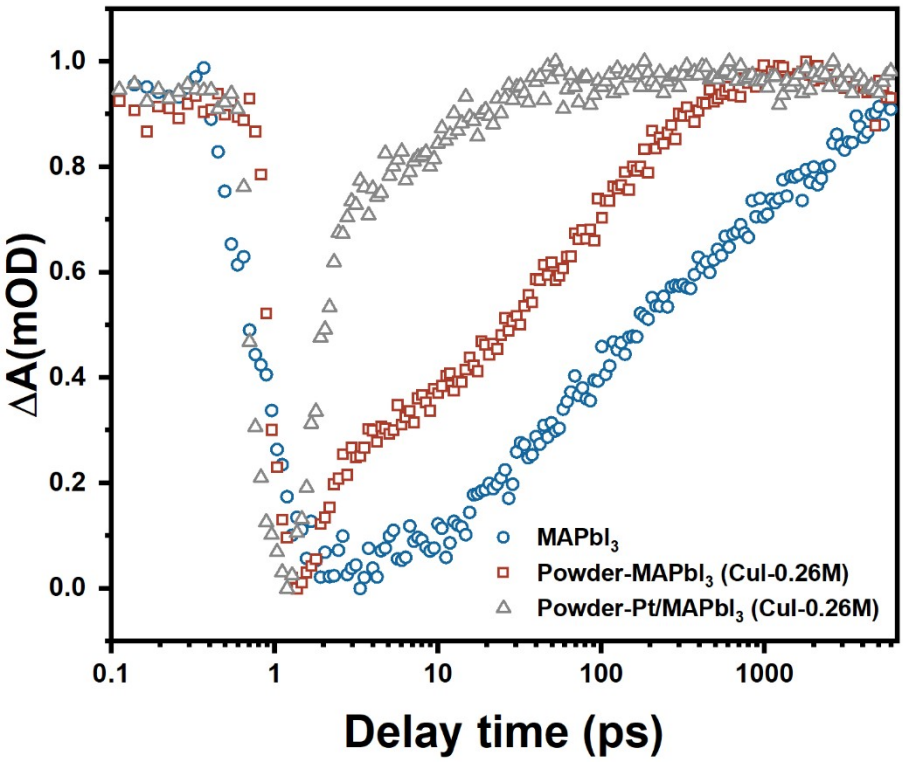


**Figure S41**. The exciton bleach kinetics of $MAPbI_3$, Powder-$MAPbI_3$ (CuI-0.26 M) and Powder-Pt (2.0 wt%)/$MAPbI_3$ (CuI-0.26 M).

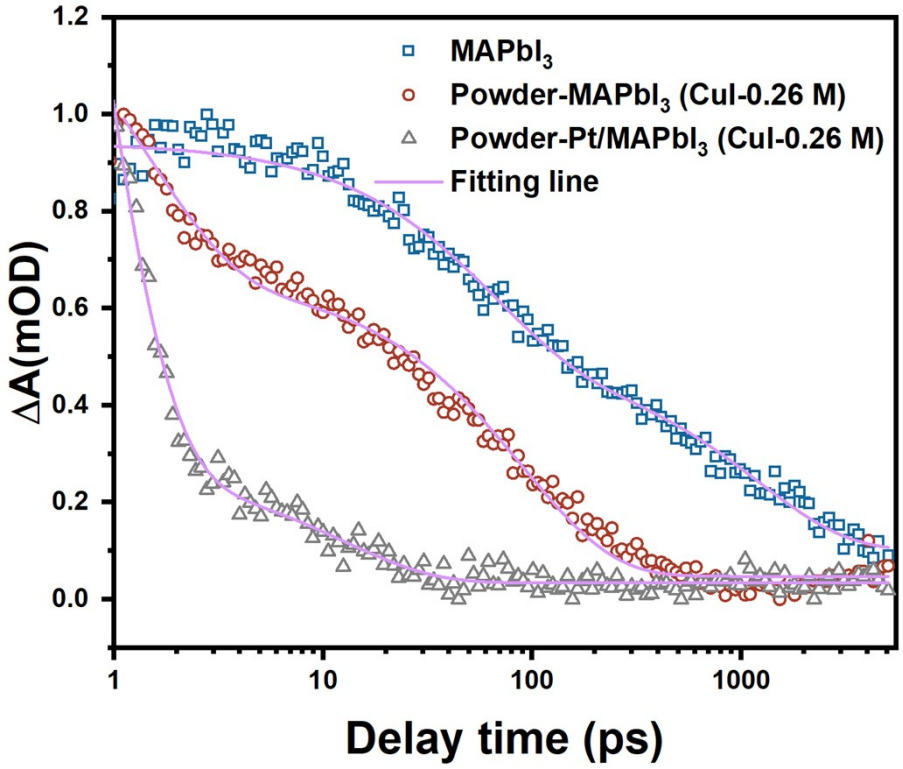


**Figure S42**. TA kinetics of the $MAPbI_3$, Powder-$MAPbI_3$ (CuI-0.26 M) and Powder-Pt (2.0 wt%)/$MAPbI_3$ (CuI-0.26 M).

**Table S1.** The mean SPV of the $MAPbI_3$, $Cu/MAPbI_3$ and $CuI/MAPbI_3$ samples under chopped 500 nm illumination.

| Sample | | Mean SPV (mV) |
|---|---|---|
| $MAPbI_3$ | $MAPbI_3$ | -16 |
| $Cu/MAPbI_3$ | Cu | -14 |
| | $MAPbI_3$ | 21 |
| $CuI/MAPbI_3$ | CuI | 5 |
| | $MAPbI_3$ | -20 |

**Table S2.** PL decay lifetime of the $MAPbI_3$ and Powder-$MAPbI_3$ (CuI-0.26 M).

| Sample | $A_1$ | $\tau_1$ (ns) | $A_1$ | $\tau_2$ (ns) | $\tau_{ave}$ (ns) |
|---|---|---|---|---|---|
| $MAPbI_3$ | 0.36 | 10.7 | 0.64 | 72.9 | 68.03 |
| Powder-$MAPbI_3$ (CuI-0.26 M) | 0.50 | 30.3 | 0.50 | 30.3 | 30.3 |

Kinetics fitting models. The time-resolved PL results of the $MAPbI_3$, Powder-$MAPbI_3$ (CuI-0.26 M) and Powder-Pt (2.0 wt%)/$MAPbI_3$ (CuI-0.26 M) are fitting to a bi-exponential decay:

$$S=A+A_1e^{-\frac{t}{\tau_1}}+A_2e^{-\frac{t}{\tau_2}} \quad (1)$$

Where A, $A_1$ and $A_2$ are constants acquired by the fitting of each decay curve. $\tau_1$ and $\tau_2$ reflect the decay components owing to bimolecular recombination and free carrier recombination, respectively. The average PL lifetime ($\tau_{ave}$) has been calculated using the above decay fitting data and the following formula:

$$\tau_{ave}=\frac{A_1\tau_1^2+A_2\tau_2^2}{A_1\tau_1+A_2\tau_2} \quad (2)$$

**Table S3.** TA decay lifetime of $MAPbI_3$ and Powder-$MAPbI_3$ (CuI-0.26 M).

| Sample | $A_1$ | $\tau_1$ (ps) | $A_1$ | $\tau_2$ (ps) | $\tau_{ave}$ (ps) |
|---|---|---|---|---|---|
| $MAPbI_3$ | 0.53 | 51 | 0.47 | 2256 | 1087.35 |
| Powder-$MAPbI_3$ (CuI-0.26 M) | 0.52 | 1.6 | 0.48 | 112 | 54.59 |

Kinetics fitting models. The TA kinetics of the $MAPbI_3$, Powder-$MAPbI_3$ (CuI-0.26 M) and Powder-Pt (2.0 wt%)/$MAPbI_3$ (CuI-0.26 M) are fitting to a bi-exponential decay:

$$S \propto A_1 e^{-\frac{t}{\tau_1}} + A_2 e^{-\frac{t}{\tau_2}} \quad (3)$$

where $A_1$, $A_2$ and $\tau_1$, $\tau_2$ are the relative amplitude and time constant. According to the relative amplitude and time constant obtained by the bi-exponential fitting, the average electron transfer, hole transfer and charge recombination time constants ($\tau_{ave}$) of the carrier is calculated by the following formula:

$$\tau_{ave} = \tau_1 * A_1 + \tau_2 * A_2 \quad (4)$$

**Table S4.** A summary of the performance and experimental parameters of reported halide perovskite photocatalysts for $H_2$ evolution.

| Catalysts | Mass of catalyst (mg) | Light source | Activity ($\mu mol\ h^{-1}$) | STH (%) | Year/ref. |
|---|---|---|---|---|---|
| $MAPbI_3$/Pt | 200 | $\lambda > 475$ nm, 100 mW $cm^{-2}$ | 11.4 | 0.81 | 2016[6] |
| $MAPbI_3$/rGO | 100 | $\lambda \geq 420$ nm, 120 mW $cm^{-2}$ | 93.9 | -- | 2018[7] |
| $MAPbI_3$-Pt/$TiO_2$ | 50 | $\lambda > 420$ nm, 200 mW $cm^{-2}$ | 89.2 | 0.86 | 2018[8] |
| $MAPbBr_{3-x}I_x$/Pt | 250 | AM 1.5G, 100 mW $cm^{-2}$ | 161.5 | 1.05 | 2018[9] |
| $Ni_3C$/$MAPbI_3$ | 50 | $\lambda \geq 420$ nm, 100 mW $cm^{-2}$ | -- | 0.91 | 2019[10] |
| $MAPbI_3$/BP | 30 | $\lambda \geq 420$ nm, 100 mW $cm^{-2}$ | -- | 0.93 | 2019[11] |
| Pt/$MA_3Bi_2I_9$ | 40 | $\lambda > 400$ nm, 100 mW $cm^{-2}$ | 6.77 | 0.48 | 2019[12] |
| $Cs_3Bi_{0.6}Sb_{1.4}I_9$ | 100 | AM 1.5G, 100 mW $cm^{-2}$ | 92.6 | 0.32 | 2020[13] |
| ML-$MoS_2$/$MAPbI_3$ | 100 | AM 1.5G, 60 mW $cm^{-2}$ | 637 | 1.09 | 2020[14] |
| Pt/$MAPbI_3$/ CA-PASA | 100 | $\lambda \geq 420$ nm, 100 mW $cm^{-2}$ | -- | 2.15 | 2020[15] |

| | | | | | |
|---|---|---|---|---|---|
| $MoS_2/MAPbI_3$ | 100 | λ > 380 nm, 450 mW $cm^{-2}$ | 206.1 | -- | 2020[4] |
| $MA_3Bi_2I_9/DMA_3BiI_6$ | 100 | 300 W Xe-lamp, λ > 420 nm | 19.82 | -- | 2020[16] |
| $MAPbI_3$/CoP | 2.5 | 300 W Xe-lamp, λ > 420 nm | 5.218 | -- | 2020[17] |
| Pt/2D-$PMA_2PbI_4$ | 150 | AM 1.5G, 100 mW $cm^{-2}$ | 120 | 1.57 | 2021[18] |
| $Ti_3C_2$ MXene/$MAPbI_3$ | 30 | λ > 420 nm, 300 mW $cm^{-2}$ | 93.7 | 0.89 | 2022[19] |
| Pt/$FAPbBr_{3-x}I_3$ | 100 | AM 1.5G, 100 mW $cm^{-2}$ | 682.6 | 4.50 | 2022[20] |
| $MoSe_2/MAPbBr_{3-x}I_x$ | 150 | λ > 420 nm, 100 mW $cm^{-2}$ | 3440 | 3.85 | 2023[21] |
| $MoS_2$/S-$PMA_2PbI_4$ | 50 | 300 W Xe-lamp, λ > 420 nm | 551.25 | 2.21 | 2024[22] |
| $MoS_2$/S-$FAPbBr_{3-x}I_3$ | 50 | 300 W Xe-lamp, λ > 420 nm | 1059 | 4.63 | 2024[22] |
| Pt/$MAPbI_3$ (CuI-0.26M) | 50 | AM 1.5G, 100 mW $cm^{-2}$ | 2310 | 5.25 | This work |

**Table S5.** The amount of Cu species in Powder-$MAPbI_3$ (CuI-0.26 M) and Powder-Pt (2.0 wt%)/$MAPbI_3$ (CuI-0.26 M) determined by ICP-OES.

| Sample | Cu (%) |
|---|---|
| Powder-$MAPbI_3$ (CuI-0.26 M) | 29.90 |
| Powder-Pt (2.0 wt%)/$MAPbI_3$ (CuI-0.26 M) | 5.89 |

**Table S6.** PL decay lifetime of the Powder-Pt (2.0 wt%)/$MAPbI_3$ (CuI-0.26 M).

| Sample | $A_1$ | $\tau_1$ (ns) | $A_1$ | $\tau_2$ (ns) | $\tau_{ave}$ (ns) |
|---|---|---|---|---|---|
| Powder-Pt$MAPbI_3$ (CuI-0.26 M) | 0.18 | 12.45 | 0.82 | 1.63 | 8.54 |

**Table S7.** TA decay lifetime of Powder-Pt (2.0 wt%)/$MAPbI_3$ (CuI-0.26 M).

| Sample | $A_1$ | $\tau_1$ (ps) | $A_1$ | $\tau_2$ (ps) | $\tau_{ave}$ (ps) |
|---|---|---|---|---|---|
| Powder-Pt$MAPbI_3$ (CuI-0.26 M) | 0.93 | 0.69 | 0.07 | 23.12 | 2.26 |

REFERENCES

1. M. G. Brik, I. V. Kityk, N. M. Denysyuk, O. Y. Khyzhun, S. I. Levkovets, O. V. Parasyuk, A. O. Fedorchuk and G. L. Myronchuk, Phys. Chem. Chem. Phys., 2014, 16, 12838-12847.

2. M. Zhang, Z. Tian, D. Zhu, H. He, S. Guo, Z. Chen and D. Pang, New J. Chem., 2018, 42, 9496-9500.

3. N. Kaisar, T. Paul, P. W. Chi, Y. H. Su, A. Singh, C. W. Chu, M. K. Wu and P. M. Wu, Materials (Basel)., 2021, 14, 5718.

4. X. Zhao, S. Chen, H. Yin, S. Jiang, K. Zhao, J. Kang, P. Liu, L. Jiang, Z. Zhu, D. Cui, P. Liu, X. Han, H. Yang and H. Zhao, Matter-US., 2020, 3, 935-949.

5. S. Gharibzadeh, B. A. Nejand, A. Moshaii, N. Mohammadian, A. H. Alizadeh, R. Mohammadpour, V. Ahmadi and A. Alizadeh, Chemsuschem, 2016, 9, 1929-1937.

6. S. Park, W. J. Chang, C. W. Lee, S. Park, H. Y. Ahn and K. T. Nam, Nat. Energy, 2017, 2, 16185.

7. Y. Wu, P. Wang, X. Zhu, Q. Zhang, Z. Wang, Y. Liu, G. Zou, Y. Dai, M. H. Whangbo and B. Huang, Adv. Mater., 2018, 30, 1704342.

8. X. Wang, H. Wang, H. Zhang, W. Yu, X. Wang, Y. Zhao, X. Zong and C. Li, ACS Energy Lett., 2018, 3, 1159-1164.

9. Y. Wu, P. Wang, Z. Guan, J. Liu, Z. Wang, Z. Zheng, S. Jin, Y. Dai, M.-H. Whangbo and B. Huang, ACS Catal., 2018, 8, 10349-10357.

10. Z. Zhao, J. Wu, Y. Zheng, N. Li, X. Li and X. Tao, ACS Catal., 2019, 9, 8144-8152.

11. R. Li, X. Li, J. Wu, X. Lv, Y. Zheng, Z. Zhao, X. Ding, X. Tao and J. Chen, Appl. Catal. B-Environ., 2019, 259, 118075.

12. Y. Guo, G. Liu, Z. Li, Y. Lou, J. Chen and Y. Zhao, ACS Sustain. Chem. Eng., 2019, 7, 15080-15085.

13. G. Chen, P. Wang, Y. Wu, Q. Zhang, Q. Wu, Z. Wang, Z. Zheng, Y. Liu, Y. Dai and B. Huang, Adv. Mater., 2020, 32, e2001344.

14. F. Wang, X. Liu, Z. Zhang and S. Min, Chem. Commun. (Camb), 2020, 56, 3281-3284.

15. Y. Zhao, Q. Zeng, Y. Yu, T. Feng, Y. Zhao, Z. Wang, Y. Li, C. Liu, J. Liu, H. Wei, S. Zhu, Z. Kang, H. Zhang and B. Yang, Mater. Horiz., 2020, 7, 2719-2725.

16. Y. Tang, C. H. Mak, R. Liu, Z. Wang, L. Ji, H. Song, C. Tan, F. Barrière and H. Y. Hsu, Adv. Funct. Mater., 2020, 30, 2006919.

17. C. Cai, Y. Teng, J. Wu, J. Li, H. Chen, J. Chen and D. Kuang, Adv. Funct. Mater., 2020, 30, 2001478.

18. H. Wang, H. Zhang, J. Wang, Y. Gao, F. Fan, K. Wu, X. Zong and C. Li, Angew. Chem. Int. Ed. Engl., 2021, 60, 7376-7381.

19. H. Li, X. Lv, R. Li, X. Tao and Y. Zheng, J. Power. Sources, 2022, 522, 213006.

20. Y. Wu, Q. Wu, Q. Zhang, Z. Lou, K. Liu, Y. Ma, Z. Wang, Z. Zheng, H. Cheng, Y. Liu, Y. Dai, B. Huang and P. Wang, Energ. Environ. Sci., 2022, 15, 1271-1281.

21. X. Liu, Q. Zhang, S. Zhao, Z. Wang, Y. Liu, Z. Zheng, H. Cheng, Y. Dai, B. Huang and P. Wang, Adv. Mater., 2023, 35, 2208915.

22. T. Xu, Y. Xie, S. Qi, H. Zhang, W. Ma, J. Wang, Y. Gao, L. Wang and X. Zong, Angew. Chem. Int. Ed. Engl., 2024, 63, e202409945.